Statistical properties of streamline geometry in turbulent wall-flows

Rina Perven,[*] Jimmy Philip,[†] and Joseph Klewicki[‡]
Department of Mechanical Engineering, University of Melbourne, VIC 3010, Australia

(Received 4 May 2020; accepted 25 January 2021; published 12 March 2021)

Complex but coherent motions form and rapidly evolve within wall-bounded turbulent flows. Research over the past two decades broadly indicates that the momentum transported across the flow largely derives from the dynamics of these coherent motions. The associated spatial organization, and its inherent connection to the dynamics, motivates the present research on streamline curvature and torsion. All the present results have been calculated and compared using the existing direct numerical simulation databases for boundary layers and channel flows. Here we have investigated the statistical properties of the local curvature (κ) and torsion (τ) of streamlines for the considered wall-bounded flows. The computation of κ (deviation from a straight line-bending) and τ (out of plane motion-twisting) uses the local construction of the Frenet-Serret coordinate frame. The analysis shows that the statistics of these geometrical properties change significantly with wall-normal position. Even though the mean wall-normal velocity is zero (e.g., for channel flow), the wall-normal curvature component shows a notable positive peak close to the wall. The correlation coefficient and the conditional average of the wall-normal velocity corresponding to the wall-normal curvature exhibit an anticorrelation between them. The probability density function of the curvatures have been calculated across the flow and compared with the κ^{-4} scaling proposed by Schaefer [J. Turbul., N28 (2012)] for both the total and fluctuating field. Although in isotropic turbulence this scaling of curvature pertains to scales that are near to and smaller than the Kolmogorov scale (η), in wall-bounded turbulence we find the onset of this scaling to occur at slightly larger length scales of $\approx 10\eta$. In fact, the start of this scaling with wall distance coincides with the three-dimensionalization of the vorticity field and agrees with the stagnation point structure in the inertial domain observed by Dallas *et al.*, [Phys. Rev. E **80**, 046306 (2009)]. In this region, the mean radius of curvature scales like the Taylor microscale. The standard deviation of torsion exhibits a decreasing trend with distance from the wall. The torsion to curvature intensity ratio reveals that the out of plane motion of the streamlines exceeds in-plane bending. The joint pdf of curvature and velocity magnitude supports the notion that large curvature values correspond to the region near a stagnation point. Furthermore, the joint pdf results between curvature components provides information about the orientation of the streamlines at different wall-normal locations.

DOI: 10.1103/PhysRevFluids.6.034609

I. INTRODUCTION

Coherent motions have long been known to populate turbulent wall-flows through a process of continual formation, evolution, and obliteration [1–3]. This spatiotemporal recurrence of motions

[*]rina1.bd@gmail.com
[†]jimmyp@unimelb.edu.au
[‡]klewicki@unimelb.edu.au

TABLE I. Inner normalized leading order balance layer thicknesses for boundary layer and channel flows.

Leading balance (boundary layer)	Leading balance (channel)	Layer thickness (channel)	Layer thickness (boundary layer)
I. $\|VF\| \simeq \|MI\|$	$\|VF\| \simeq \|PG\|$	$0 \lesssim y^+ \lesssim 4$	$0 \lesssim y^+ \lesssim 4$
II. $\|VF\| \simeq \|TI\|$	$\|VF\| \simeq \|TI\|$	$4 \lesssim y^+ \lesssim 1.6\sqrt{\delta^+}$	$4 \lesssim y^+ \lesssim 2.2\sqrt{\delta^+}$
III. $\|VF\| \simeq \|TI\| \simeq \|MI\|$	$\|VF\| \simeq \|TI\| \simeq \|PG\|$	$1.6\sqrt{\delta^+} \lesssim y^+ \lesssim 2.6\sqrt{\delta^+}$	$2.2\sqrt{\delta^+} \lesssim y^+ \lesssim 3.6\sqrt{\delta^+}$
IV. $\|TI\| \simeq \|MI\|$	$\|TI\| \simeq \|PG\|$	$2.6\sqrt{\delta^+} \lesssim y^+ \lesssim \delta^+$	$3.6\sqrt{\delta^+} \lesssim y^+ \lesssim \delta^+$

is related to identifiably recognizable spatial organization and similar evolutionary features. An intriguing motivation for deeper investigation is associated with the potential to use these motions, in some systematic manner, as a basis for simplified descriptions that capture the essential elements of wall-flow dynamics [4,5]. Indeed, in a statistical sense, this underlying spatial organization leads many to strongly suspect that the long-recognized self-similar scaling properties of turbulent wall flows connects the geometry and dynamics of the instantaneous motions [6]. As with many studies of turbulence, a primary gap in our present understanding pertains to the connections between statistical behaviors of the geometry and the underlying instantaneous dynamics. The present study addresses aspects of this knowledge gap by quantifying statistical properties associated with the differential geometry measures of curvature and (to a much lesser degree) torsion of the streamline patterns in turbulent boundary layer and channel flows.

Streamlines are defined by curves that are instantaneously tangent to the velocity of the flow. Curvature measures the deviation from a straight line while torsion quantifies the out of plane motion of a curve. A broad aim here is to clarify the connections between geometry and dynamics, and the degree to which they are reflected in the instantaneous motions. As such, important ingredients of the present study draw upon (1) the leading order mean force balance in turbulent wall-flows, (2) the previously documented behavior of streamline curvature probability density function in isotropic turbulent flows [7], and (3) the characteristic length scales and the geometric and scaling implications associated with the distributions of stagnation points in the fluctuating velocity field [8].

A. Mean dynamical structure and its geometric implications

Analysis of the Reynolds Averaged Navier-Stokes (RANS) equations, as simplified for the canonical turbulent wall-flows reveals a layer structure associated with the leading order balances with distance from the wall [9,10]. For the flat plate boundary layer and fully developed channel (or pipe) flows, the mean momentum balance (MMB) equations have three terms. In the boundary layer, the three terms are mean inertia, turbulent inertia (gradient of the Reynolds shear stress), and the mean viscous force. These are respectively denoted MI, TI, and VF. For channel flow, the TI and VF terms are also present, but the MI term is replaced by the mean pressure gradient (PG). In either case, different terms balance each other at varying distance from the wall.

As shown in Table I, the layer structure associated with the leading balances in the MMB is qualitatively different from the classical viscous sublayer, buffer layer, logarithmic and wake layer description that derives from the observed features of the mean velocity profile [9,11]. A central distinction between the classical versus MMB based descriptions (apart from the latter having a direct basis in the RANS equations) pertains to the onset and scaling properties of the physical space *inertial sublayer* that is a primary focus in many experimental and theoretical studies [2,3]. In the classical description, one surmises that viscous effects become subdominant beginning at a distance that is $y = O(\nu/u_\tau)$ from the wall (typically around $y^+ = yu_\tau/\nu = 100$), where the friction velocity is defined by $u_\tau = \sqrt{\tau_w/\rho}$, with τ_w denoting the mean wall shear stress, and ν and ρ respectively denoting the kinematic viscosity and mass density of the fluid [3]. In the

MMB-based description, the loss of a leading order VF is found to occur at a wall-normal position $y \propto \sqrt{\nu\delta/u_\tau}$ (or equivalently, $y^+ \propto \sqrt{\delta^+}$), where δ in Table I denotes either the half-channel height or the boundary layer thickness. (Herein, the boundary layer δ is determined using the composite profile formulation of Chauhan *et al.* [12].) This square root Reynolds number dependence is experimentally supported by measurements of the terms in the MMB, and analytically via multiscale treatment of the MMB [9,10,13]. This first appearance of inertially dominated flow is additionally supported by measurements of the logarithmic layer onset at high Reynolds number [14].

The self-similar spatial structure admitted by the MMB equations [6] is of inherent interest owing to its potential connection to the underlying geometry of the turbulence. A key finding here is that the mean equations formally admit an invariant form across a hierarchy of scaling layers. The widths of the members of this layer hierarchy span from $O(\nu/u_\tau)$ to $O(\delta)$, as do the wall-normal locations of these layers. Importantly, the y coordinate stretching function (required to generate the invariant self-similar form of the MMB) becomes a linear function of distance from the wall on the inertial sublayer (i.e., beyond layer III) [11]. This analytical result underpins the existence of a formally admitted similarity solution to the mean equations that is shown to recover the classical logarithmic mean velocity profile equation as $\delta^+ \to \infty$ [10,15]. These and related analytical properties also support the existence of, and evidence for, self-similar behaviors of the velocity field motions on the inertial sublayer [16,17]. In the present study, we examine streamline curvature and torsion statistics in this context.

Physically, the layer widths on the hierarchy represent a characteristic length scale of the motions responsible for wallward momentum transport, and this motivated more detailed analyses of the spatial structure of the negative Reynolds stress fluctuations. These investigations [6,18] revealed intriguing observations suggesting that the slope of the mean velocity profile on the inertial sublayer (as quantified by the von Kármán constant) relates to the space-filling properties of the negative Reynolds stress motions, and further that the amplitude and scale of these motions are self-similarly related. Alternatively, the inward flux of momentum can be equivalently viewed as being associated with the outward transport of vorticity [19,20]. Near the wall, the flow dynamics are strongly coupled to the mechanisms of vorticity stretching and reorientation, which serve to rapidly three-dimensionalize the vorticity field. With increasing y, however, advection becomes the primary mechanism for vorticity transport and is characterized by the spatial dispersion of small scale regions of intense vorticity [21,22]. In the present study, the mean curvature statistics reflect evidences of this feature of the vorticity stretching behavior from the high turbulence region close to the wall to the outer edge of layer II. With increasing y this behavior is similarly shown to correlate with the decreasing density of stagnation points in the fluctuating velocity field (described relative to the studies of Vassilicos *et al.* [8,23] below), as well as the statistical properties of the fluctuating streamline curvature documented herein.

B. Previous studies of streamline geometry

Previous researchers have studied turbulent flows relative to both streamlines [7,24] and particle trajectories [25,26]. We note that the addition of a constant velocity to the flow field will not change the intrinsic properties of a streamline, such as curvature and torsion (to be defined below), nor would it change the Navier-Stokes equations, which is the basis of Galilean invariance. However, Galilean invariance cannot be employed to obtain one flow field from another, when there is a fixed boundary; for example, a plane Couette flow is not simply an addition of a constant velocity to plane Poiseuille (channel) flow. Here the Galilean invariance is said to be "broken" due to the no-slip boundary condition at the wall [27], which remains true for streamlines too. Nevertheless, streamline properties with zero mean velocity is extensively studied in isotropic turbulence. In our case of wall-turbulent flows, we study streamlines both from instantaneous velocity field, as well as from fluctuating (mean subtracted) velocity fields (to compare against isotropic streamline results).

For particle trajectories, Braun *et al.* [25] show that the product of curvature and velocity is linearly correlated with the vorticity, suggesting that the region of large curvature are associated

with large vorticity. Again, for particle paths, Scagliarini [26] studied the geometric properties of Lagrangian trajectories for homogeneous and isotropic turbulence. According to this study, the instantaneous curvature statistics are dominated by the flow reversals corresponding to large eddies in the flow, where the velocity magnitude assumes very low values. The joint statistics of curvature and torsion in his study highlight the coherent geometrical structure of intense vortical motion in turbulent flows that are dominated by helical-type trajectories. We should mention here that curvature of particle trajectories and streamlines essentially differ due to the partial time derivative of the velocity vector [25], and the turbulence properties would be different if considered along a streamline or pathline [28].

For defining the turbulent structures at the small scales, the entire DNS flow field was decomposed by Peters *et al.* [24] into the planar geometrical unit that they called a dissipation element. A dissipation element is defined as the spatial region containing all positions (grid points in a DNS) whose streamline trajectories can share the same pair of maximal and minimal points in velocity magnitude. The spatial properties of the turbulent fields have been structured by the streamline segment analysis by Wang [29]. He defined a streamline segment as the part of a streamline bounded by two adjacent extremal points of the velocity magnitude, and lying on the dissipation element. The mean length of these streamline segments were found to be the order of the Taylor microscale [29]. These local extreme points of velocity magnitude also include stagnation points, and coincide with minima in the turbulent kinetic energy. In the present study, we find that large curvature values are connected with low values of the velocity magnitude, i.e., stagnation region.

The most relevant work to the present research is the study by Schaefer [7]. He showed that the advection terms in the Navier-Stokes equation can be expressed in terms of streamlines curvature. Schaefer treated the curvature and torsion as field variables, and considered the case of low Reynolds number isotropic flows. In contrast, the present work considers the curvature and torsion in wall-bounded turbulent flows. Schaefer's research demonstrated that the probability density function of curvature $P(\kappa)$ follows a power-law scaling of κ^{-4} for extreme curvature values. This finding is observed herein, but not over the entire flow domain. The exponent of -4 scaling derives from the curvature being directly proportional to the product of the inverse of the velocity magnitude ($|V|^{-1}$) and the gradient of the velocity magnitude in the streamline direction. Under the assumption that the pdfs of the two products are independent and that the three velocity components are Gaussian random variables, a scaling of the pdf of the inverse absolute velocity, $|V|^{-1} =: \mathfrak{a}$, can be found for isotropic flow. It can be then shown that the pdf of the turbulence kinetic energy $\mathfrak{K} = u_i u_i/2$ follows a chi square (χ^2) distribution with three degrees of freedom. This leads to $P(\mathfrak{K}) \propto \mathfrak{K}^{1/2} e^{-\mathfrak{K}/2}$, and therefore, $P(\mathfrak{a}) \propto \mathfrak{a}^{-4} e^{-\mathfrak{a}^{-2}}$. Following this, the pdf of the absolute value of curvature can be shown to exhibit κ^{-4} behavior. The present curvature pdfs are analyzed with respect to this, and in particular the dependence of -4 scaling on wall-normal distance is clarified.

C. Stagnation point structure in turbulent wall-flows

Motivated by earlier investigations of the zero-crossing properties of velocity fluctuations and their derivatives [30,31], Vassilicos and co-workers studied the properties of the zeros (stagnation points) of the fluctuating velocity magnitude in turbulent channel flows [8,23]. Stagnation point is defined to coincide with where the fluctuating velocity components are near zero [8]. Dallas *et al.* [8] found that the distance between these stagnation points is proportional to the Taylor microscale. In the inertial sublayer (inner part of layer IV in Table I), they also showed that the number density of the stagnation points is inversely proportional to the wall-normal distance. Since these results from Dallas *et al.* [8] are pertinent to the present work, we briefly outline their derivation using a slightly simplified argument than in Ref. [8]. From the standard results (e.g., Refs. [31,32]) on the zero-crossing of a one-dimensional mean-subtracted random signal (u), it known that the number of zero-crossing per unit length (x) is proportional to $\sqrt{(du/dx)^2/\sigma_u} \sim 1/\lambda$, where σ_u is the signal variance. A 3D analog version leads to the number of stagnation points per unit volume (N_0) in three dimensions proportional to $1/\lambda^3$, appropriate for isotropic turbulence. In wall flows, Dallas *et al.* [8]

consider (or more accurately said, assume) that the $N_0 \sim 1/(\lambda^2\delta_\nu)$, where the in-plane $(x-z)$ density is proportional to $1/\lambda^2$; however, the thickness is taken proportional to the viscous scale δ_ν. Now, we know that in the inertial region (also see Sec. III A) $\lambda^+ := \lambda/\delta_\nu \sim \sqrt{y^+}$ (where $y^+ = y/\delta_\nu$), which implies that stagnation point density per unit volume in viscous units: $N_0^+ := N_0/(1/\delta_\nu^3) \sim 1/\lambda^2 \sim 1/y^+$.

In the present study, we explore the onset of -4 scaling (related to extreme curvature values that naturally occur in stagnation regions) as well as the variations in radius of curvature with the wall-normal distance.

The above background literature connects to the present study. The reorientation of the mechanism for vorticity stretching and advection studied by Klewicki [11] is reflected by the present mean curvature statistics. As analyzed by Schaefer [7], the curvature values are extreme in stagnation regions and the -4 exponent scaling is likely related to the turning of the streamlines around these points. According to the studies by Vassilicos and others [8,23], the number density of the stagnation points decrease with y^+ in the inertial domain where the distance between stagnation points is proportional to the Taylor microscale. The present study will show that unlike the onset of -4 scaling that occurs in isotropic turbulence at a curvature that varies in a similar trend to the inverse of the Kolmogorov length scale, in wall-turbulence the κ^{-4} scaling starts at a slightly larger length scale. Furthermore, the onset of the scaling approximately follows a power-law scaling with y^+ on the inertial domain, whereas in the same domain the mean radius of curvature nominally scales with the Taylor microscale.

II. CALCULATION OF CURVATURE AND TORSION

The present analysis employs three DNS data sets. These include boundary layer data at friction Reynolds numbers $\delta_{99}^+ \approx 1310$ and $\delta_{99}^+ \approx 2000$ [33] (where δ_{99} is the boundary layer height where mean velocity is the 99% of the free stream velocity), and channel flow data at friction Reynolds number $\delta^+ \approx 934$ [34]. Here, in the case of the boundary layer, δ^+ was found to be about 1660 and 2530 when the boundary layer thickness δ was computed using the composite profile formulation by Chauhan *et al.* [12]. The streamwise, spanwise, and wall-normal directions are considered to be along the x-axis, z-axis, and y-axis, respectively. For the channel flow, it is feasible to compute statistics over the entire plane owing to its horizontally homogeneous fully developed properties. The boundary layers, however, required the use of smaller domains to approximate a constant friction velocity condition. For this reason, the slices of only 312 grid points are considered in the x-direction and 2048 grid points are taken in the z-direction, corresponding to $(x/\delta \times z/\delta) \approx (0.78 \times 3)$ at 38 wall positions for $\delta^+ = 2530$ boundary layer. Similarly 195 and 4096 grid points in x and z [i.e., $(x/\delta \times z/\delta) \approx (0.79 \times 9.6)$] respectively at 36 wall-positions in the case of $\delta^+ = 1660$ boundary layer. For comparison, 312 and 2048 grid points are considered in x and z [i.e., $(x/\delta \times z/\delta) \approx (2.55 \times 8.4)$] respectively at 37 wall-positions for $\delta^+ = 934$ channel DNS as well. Statistics are computed from the average of six independent DNS fields by averaging over the planar domains indicated above.

A. Method for calculating streamlines

To colocate the curvature and torsion values with the grid points, streamline segments local to each grid point were computed. A fourth-order Runge-Kutta method was employed to calculate the streamline segments through each grid point location and from these the local curvature and torsion were computed. The step size that defines the space between two consecutive points on the streamline segment was tested over a wide range of values and a value for which the statistics remain fixed was employed. Finally, a pseudo-time-step size of 0.001 viscous units has been used for all three cases. To put this in context, with the mean centerline velocity of about $U^+ \approx 20$, the spatial distance is about 0.02 viscous units, which is considerably smaller than the DNS grid spacing.

B. Frenet-Serret apparatus

The Frenet-Serret apparatus is an orthogonal coordinate system defined locally along a space curve, and is used herein as a basis for computing the curvature and torsion of the streamlines [35]. These tools relate the three basic vectors of differential geometry; the tangent vector **T**, normal vector **N**, and binormal vector **B**, as well as two scalar quantities: curvature κ and torsion τ. Here **T** is a unit vector pointing in the direction of the velocity vector, **N** is a unit vector pointing in the direction of the streamline gradient of **T**, and **B** is the unit vector that is orthogonal to both **T** and **N**. Curvature quantifies the bending of a curve from a straight line within a reference plane. Thus, for example, the curvature value for a straight line is zero, and that of a circle of radius r is constant and equal to $1/r$. The torsion measures the out-of-plane motion of a curve, i.e., the twisting motion of the curve.

The Frenet-Serret tools are for a unit speed curve $\boldsymbol{\beta}(s)$, and, the relation between **T**, **N**, **B**, κ, and τ are given by

$$\frac{d\mathbf{T}}{ds} = \kappa\mathbf{N}, \tag{1}$$

$$\frac{d\mathbf{N}}{ds} = -\kappa\mathbf{T} + \tau\mathbf{B}, \tag{2}$$

$$\frac{d\mathbf{B}}{ds} = -\tau\mathbf{N}, \tag{3}$$

where, s the streamline arc length.

In terms of the arc or pseudo-time parameter that varies along the streamline, the equation for the tangent of the streamline is given by

$$\mathbf{T} = \frac{\dot{\boldsymbol{\beta}}}{|\dot{\boldsymbol{\beta}}|}, \tag{4}$$

where $\dot{\boldsymbol{\beta}}$ is the pseudo-time derivative of arc $\boldsymbol{\beta}$. Subsequent use of the Frenet-Serret equations (1)–(3), along with the fact that $\dot{s} = |\dot{\boldsymbol{\beta}}|$, gives the final equations for κ and τ as

$$\kappa = \frac{|\dot{\boldsymbol{\beta}} \times \ddot{\boldsymbol{\beta}}|}{|\dot{\boldsymbol{\beta}}|^3} \tag{5}$$

and

$$\tau = \frac{[\dot{\boldsymbol{\beta}}, \ddot{\boldsymbol{\beta}}, \dddot{\boldsymbol{\beta}}]}{|\dot{\boldsymbol{\beta}} \times \ddot{\boldsymbol{\beta}}|^2}. \tag{6}$$

The derivatives in Eqs. (5) and (6) were computed using standard central difference formulas. Following Schaefer [7], the curvature components can be defined by

$$\kappa_i \equiv \kappa N_i = \frac{dT_i}{ds}, \tag{7}$$

where, dT_i/ds [$i = 1, 2, 3$ (x, y, z)] is the derivative of the tangent vector components in the coordinate directions. Accordingly,

$$\kappa = \sqrt{\left(\kappa_x^2 + \kappa_y^2 + \kappa_z^2\right)} \tag{8}$$

is the curvature magnitude. Note that the curvature values in Eqs. (5) and (8) are the same. We primarily choose Eq. (8) for curvature calculation since from (7), one can consider the curvatures components individually.

III. STATISTICAL PROPERTIES OF CURVATURE AND TORSION

A. Curvature

In a turbulent flow, the streamline pattern changes from one instant to the next. Thus, the curvature components in the streamwise, wall normal, and spanwise directions, $\kappa_x, \kappa_y, \kappa_z$ respectively, at any given point in space are fluctuating quantities. For this reason, we investigate the statistical properties of κ and τ, e.g., the mean ($\overline{\kappa_i} = \sum \kappa_i/N$) and the standard deviation ($\sigma_{\kappa_i} = \sqrt{\sum (\kappa_i - \overline{\kappa})^2/N}$), where N is the size of the ensemble and an over-line denotes the ensemble average. In what follows, u, v and w are the fluctuating streamwise x, wall-normal y, and spanwise z velocity components. Quantities normalized by kinematic viscosity ν and friction velocity u_τ are denoted with a superscript $+$, e.g., $u^+ = u/u_\tau$, $\kappa^+ = \kappa\nu/u_\tau$, etc. The total, mean, and fluctuating streamwise velocity components are defined as $\tilde{u}$, U, and u, respectively, i.e., $\tilde{u} = U + u$, and similarly for the wall-normal and spanwise components. The curvatures computed from the total and fluctuating field are defined as $\tilde{\kappa}$ and κ, respectively.

Large values of curvature are associated with the small length scale features of the turbulent flow and vice versa. As such it can be reasoned that curvature tends to attain large values around a stagnation region either in a fixed frame for a zero mean flow field or relative to a mean flow [7]. Although a connection between stagnation regions and extreme curvature values would be sought in Sec. III D employing joint probability density functions, we begin by considering mean statistics. Interestingly, the aforementioned finding of Dallas *et al.* [8] indicates that the distance between stagnation points is proportional to the Taylor microscale. Therefore, in the present study with wall-bounded flow, we compare the inverse of the Taylor microscale with the curvature magnitude (inverse of the radius of curvature). In wall-turbulence, the Taylor microscale nominally scales with $\sqrt{y}$ in the inertial layer, as now described.

Classical theoretical analysis of the turbulence energy equation in wall-flows indicates that the energy production $\wp = \overline{uv}\partial U/\partial y$ is approximately equal to the dissipation rate ϵ in the inertial (logarithmic) layer [36], i.e, $\epsilon \approx \wp = \overline{uv}\partial U/\partial y$. On the other hand, for $y^+ \gtrsim 30$ the dissipation rate can be reasonably obtained from the isotropic estimate, $\epsilon_{iso} = 15\nu\sigma_u^2/\lambda^2$, where λ is the Taylor microscale and σ_u is the standard deviation of u. Assuming $U^+ = 1/k\ln(y^+) + B$, $\wp = \overline{uv}\partial U/\partial y \approx u_\tau^3/ky = \epsilon = 15\nu\sigma_u^2/\lambda^2$, where k is the von Kármán constant. From this (and noting that $\sigma_u \sim u_\tau$), it is apparent that λ^+ scales according to $\sqrt{y^+}$ on the logarithmic layer of wall-flows.

Herein the Taylor microscale, λ, is evaluated in two ways: based on the isotropic approximation and using the actual viscous dissipation rate. Note that there more ways to define Taylor microscale, using derivatives in different directions, or using the turbulent kinetic energy. Here, however, we satisfy ourselves with two more common definitions. The actual viscous dissipation rate $\epsilon = 2\nu\overline{s_{ij}s_{ij}}$, with $s_{ij} = (1/2)(\partial u_i/\partial x_j + \partial u_j/\partial x_i)$. Using the relation for the dissipation rate in isotropic turbulence, $\epsilon_{iso} = 15\nu\overline{(\partial u_1/\partial x_1)^2}$ or $\epsilon_{iso} = 15\nu\sigma_u^2/\lambda^2$, e.g., [36]. Thus, the Taylor microscale for isotropic turbulence can be defined as

$$\lambda = \frac{\sigma_u}{\sqrt{\overline{(\partial u_1/\partial x_1)^2}}}, \tag{9}$$

and the Taylor microscale using the actual viscous dissipation rate is

$$\lambda_\epsilon = \sqrt{\frac{15\nu}{\epsilon}}\sigma_u. \tag{10}$$

Any given instantaneous streamline gives curvatures in all three directions. Before presenting mean curvature profiles, it is important to recognize that the mean of the curvature magnitude and component curvatures are not determinable from the mean streamlines. Rather, the quantities must be computed using the instantaneous velocity field. For example, the mean wall-normal velocity V for the channel flow is identically zero (and $V \neq 0$ in a boundary layer flow), but the mean of the curvature component associated with the wall-normal direction is nonzero, as described

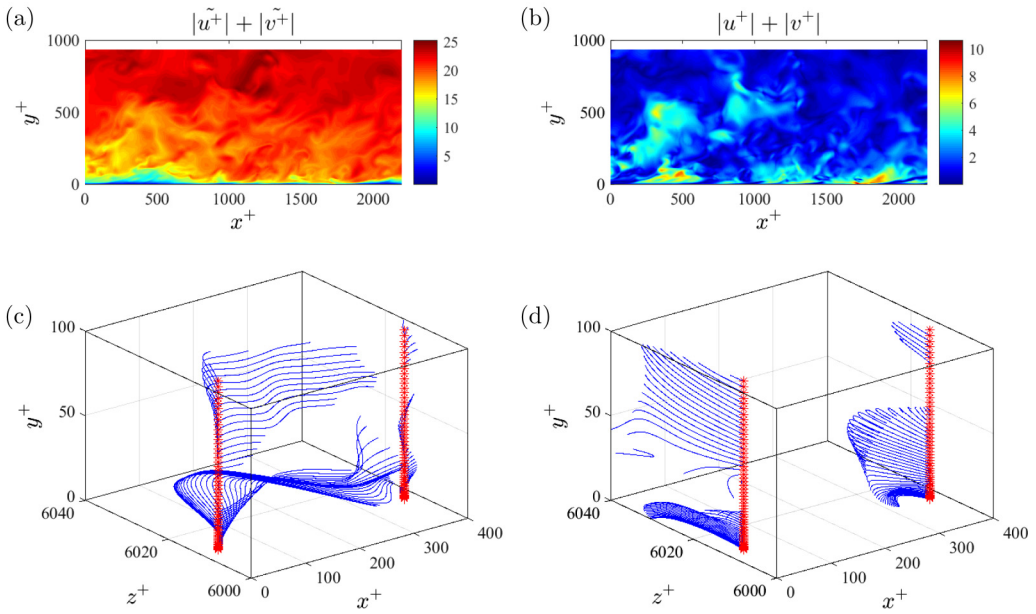

FIG. 1. (a) Contours of the total velocity field; (b) contours of the fluctuating velocity field; (c) streamlines for the total velocity field; (d) streamlines for the fluctuating velocity field.

and discussed later. This is because when the mean wall-normal curvature is computed from the instantaneous field and is nonlinearly related to the mean field. Later in the paper, we will also evaluate curvature from the fluctuating flow field. We reiterate that mean curvature values evaluated from the instantaneous and fluctuating velocity fields are denoted by $\overline{\tilde{\kappa}}$ and $\overline{\kappa}$ respectively.

Figure 1 shows examples of instantaneous velocity field contours (planar view) with the corresponding streamline patterns for the total (left side) and the fluctuating field (right side) fields. These plots visualize the different streamline patterns for the total velocity field and the mean subtracted, i.e., fluctuating velocity field. This change of the streamline pattern quantitatively affects the total and component curvature that will be discussed later at the pdfs' profiles in Fig. 7. In the following, first we will describe the statistics using total velocity field, and then from Sec. III B onwards we would include results from fluctuation velocity field where necessary. We reiterate that the results using total and fluctuating fields are distinguished using the tilde (˜) symbol. For example, $\tilde{\kappa}$ and κ are the symbols for streamline curvature from total and fluctuating velocity fields, respectively.

1. Mean curvature

Figure 2 presents the mean curvature statistics for the boundary layer and channel flows investigated. The vertical gray dashed lines in Fig. 2 indicate the position of the momentum balance layer boundaries associated with the $\delta^+ = 1660$ (Table I) flow. Figure 2(a) shows profiles of the mean curvature magnitude $\overline{\tilde{\kappa}^+}$ versus y^+ using filled symbols on a log-log scale. For comparison, we also plot the inverse of the inner normalized Taylor microscales given by (9) (denoted by the dotted line) and (10) (denoted by the dashed-dotted line). Here $\overline{\tilde{\kappa}^+}$ decreases with wall-normal distance, except in layer II between $y^+ \simeq 15$ and $y^+ \simeq 50$. This feature is discussed further relative to Fig. 2(c) below. From there $\overline{\tilde{\kappa}^+}$ exhibits an approximate power-law decrease and continues this decrease into the inertial layer (layer IV). The power-law slope is about -0.5, which is the value expected if $\overline{\tilde{\kappa}^+}$ scales like the estimate for $1/\lambda^+$ indicated above. These results indicate that the streamlines having the largest mean curvature are located close to the wall.

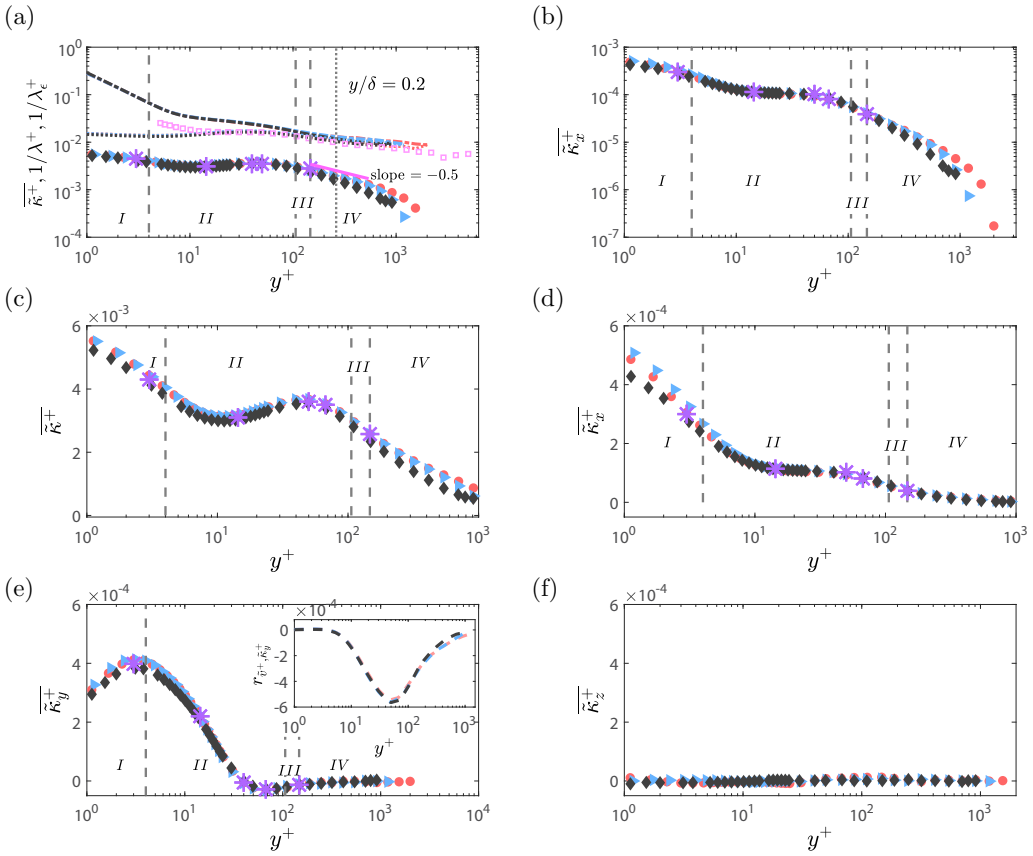

FIG. 2. Mean statistics of curvature in case of the boundary layer (colored) (Red circle, for $\delta^+ \approx 2530$ and blue triangle, for $\delta^+ \approx 1660$) and the channel flow (black diamond, for $\delta^+ \approx 934$). The vertical gray dash lines, represent the layer boundaries associated with the mean momentum equation (Table I) corresponding to $\delta^+ = 1660$. Purple star are some positions where the pdfs have been calculated that are shown in Fig. 7. (a) Mean of curvature magnitude along with the inverse of Taylor microscale [dot symbol, using Eq. (9) and dash dot symbol, using Eq. (10)]. Pink square symbol is the Taylor microscale evaluated from the experimental data of Ref. [38] for $\delta^+ \approx 6430$. Vertical dot line, denotes the wall-normal position at 0.2δ for $\delta^+ = 1660$. (b) Mean streamwise curvature. (c) The mean of curvature magnitude in log-linear scale. (d) The mean streamwise curvature in log-linear scale. (e) Mean wall-normal curvature. The inset represents the correlation of the wall-normal curvature with the wall-normal velocity. (f) Mean spanwise curvature.

The mean curvature magnitude is further compared with the Taylor microscales in Fig. 2(a). It is difficult to measure the s_{ij} tensor experimentally. Hence, for practical reasons, the isotropic estimate is often employed. This isotropic approximation works well away from the near-wall region [37], and this is also evidenced in Fig. 2(a). Here the difference between the profiles of $1/\lambda$ and $1/\lambda_\epsilon$ near the wall is clearly evident. These profiles then merge beginning near the outer portion of layer II. The experimental data by Vincenti *et al.* [38] (at $\delta^+ \approx 6430$) shown by empty square symbols also merge with the $1/\lambda$ and $1/\lambda_\epsilon$ profiles from the same position in layer II and into the outer region.

The gray vertical dotted line of Fig. 2(a) displays the $y/\delta = 0.2$ upper bound for the classical log layer at $\delta^+ = 1660$. The mean curvature magnitude at this location is not proportional to $1/\lambda^+$. The decay rate of $1/\lambda^+$ is about -0.3 that is somewhat different from the $\overline{\tilde{\kappa}^+}$ slope of about -0.5. This $1/\lambda^+$ slope deviates from the estimates of high Re log-region. Thus, in the inertial region, the radius

of curvature $(1/\overline{\tilde{\kappa}^+})$ has a power law that varies close to that of λ^+ but with a somewhat different magnitude. A similar result is also evidenced in Figs. 9 and 11 later using fluctuating velocity field.

We now investigate the wall-normal profiles of the mean curvature components. Figure 2(b) displays the mean streamwise curvature $(\overline{\tilde{\kappa}_x^+})$ with y^+. Similar to $\overline{\tilde{\kappa}^+}$, $\overline{\tilde{\kappa}_x^+}$ shows a decreasing behavior with increasing distance from the wall and an approximate power-law decrease across layer IV. In the region between $15 \lesssim y^+ \lesssim 50$, however, the $\overline{\tilde{\kappa}_x^+}$ profile is nearly constant, which is clearer when we plot $\overline{\tilde{\kappa}_x^+}$ versus y^+ on a linear-log scale as shown in Fig. 2(d). With increasing distance from the wall, the instantaneous streamlines increasingly align in the x-direction, and thus the largest $\overline{\tilde{\kappa}_x^+}$ values occur close to the wall.

Figures 2(c) and 2(d) respectively show $\overline{\tilde{\kappa}^+}$ and $\overline{\tilde{\kappa}_x^+}$ on a log-linear scale. As noted above, the mean curvature magnitude in Fig. 2(c) shows a clear increasing behavior between $y^+ \simeq 15$ and $y^+ \simeq 50$, i.e., from the peak in the turbulence kinetic energy to close to the region where advection begins to dominate vorticity transport [11]. The intermediate rise of $\overline{\tilde{\kappa}^+}$ in the region $15 \lesssim y^+ \lesssim 50$ is consistent with the lifting and roll-up of near-wall shear layer-like motions; e.g., Refs. [39,40]. In this region, vorticity stretching is large, and we expect this mechanism to reduce the scale of intense vortical motions. Beyond $y^+ \simeq 50$ advection disperses vorticity, and this transport mechanism increasingly dominates with increasing y^+ [11,41]. Consistent with this, the curvature values decrease for $y^+ \gtrsim 50$.

The behavior of the mean curvature components in the x, y and z directions in Figs. 2(d)–2(f) are different from the mean curvature magnitude $\overline{\tilde{\kappa}^+}$ in Fig. 2(c). In particular, $\overline{\tilde{\kappa}_x^+}$ in Fig. 2(d) shows a constant plateau in the region where $\overline{\tilde{\kappa}^+}$ increases in Fig. 2(c). On the other hand, $\overline{\tilde{\kappa}_y^+}$ (Fig. 2(e)) shows decreasing behavior across that region, while $\overline{\tilde{\kappa}_z^+}$ [Fig. 2(f)] is zero everywhere. The $\overline{\tilde{\kappa}_y^+}$ result is reconsidered below to investigate the origin of its nonzero values in the region close to the wall. The mean spanwise curvature $(\overline{\tilde{\kappa}_z^+})$ values in Fig. 2(f) are essentially zero for all y^+ locations. Note that these zero values of $\overline{\tilde{\kappa}_z^+}$ are not a consequence of the spanwise homogeneity, since if they were then $\overline{\tilde{\kappa}_x^+}$ in Fig. 2(b) would also be zero for fully developed channel flow. Here this zero results arise from the positive-negative symmetry of the flow. These component-wise comparisons indicate that Fig. 2(c) cannot be determined as a composite of Figs. 2(d), 2(e), and 2(f) because they are nonlinearly related. In the following section we focus on the peculiar behavior of $\overline{\tilde{\kappa}_y^+}$.

Before proceeding, we should point out that the mean curvature statistics presented above as well as the other related statistics that are evaluated further in the paper are broadly similar for both boundary layer and channel flow cases. Therefore, in the rest of the paper we will rarely comment on the small differences observed between the two flow types, and for brevity we will show only one flow type in some sections below.

2. Behavior of the wall-normal component of curvature near the wall

The mean wall-normal curvature $(\overline{\tilde{\kappa}_y^+})$ in Fig. 2(e) exhibits a positive peak near the outer edge of layer I and a slightly negative peak near the outer edge of layer II. In layer IV, the $\overline{\tilde{\kappa}_y^+}$ profiles are close to zero. For channel flow, $\overline{\tilde{\kappa}_y^+} \neq 0$ even though $V = 0$ everywhere. This is because the mean wall-normal curvature component for the instantaneous flow field is not directly determined by the corresponding wall-normal velocity component. Rather, $\tilde{\kappa}_y$ depends not only on the fluctuating wall-normal velocity, but also on the other fluctuating velocity components. These effects are further clarified in Sec. III B on the pdf.

Nevertheless, we expect the instantaneous wall-normal velocity to have a significant effect on the wall-normal curvature. Therefore, the inset plot of Fig. 2(e) presents the correlation between $\tilde{\kappa}_y$ and $\tilde{v}$ versus y^+. Here the correlation function is given by

$$r_{\tilde{v},\tilde{\kappa}_y} = \frac{1}{N}\sum_{i=1}^{i=N}(\tilde{v} - V)(\tilde{\kappa}_y - \overline{\tilde{\kappa}_y}), \tag{11}$$

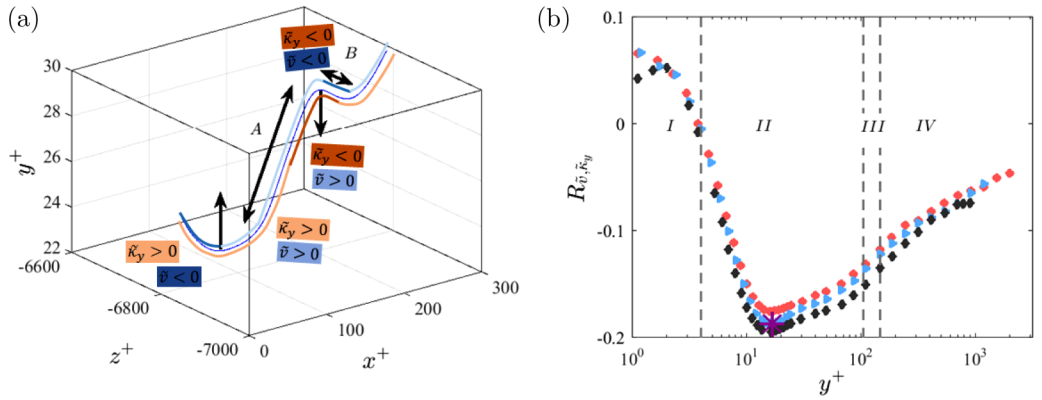

FIG. 3. (a) Configuration that depicts positive κ_y near $y^+ = 24$. The up and down arrows denote the local radius of curvature and the sign of κ_y relative to the indicated minimum wall-normal location of the streamline. The inclined double arrows at "*A*" and "*B*" indicate the inflectional regions on this streamline. (b) The correlation coefficient of $\tilde{v}^+$ and $\tilde{\kappa}_y^+$ in case of the boundary layer (colored) (Red circle, for $\delta^+ \approx 2530$ and blue triangle, for $\delta^+ \approx 1660$) and the channel flow (black diamond, for $\delta^+ \approx 934$). The vertical gray dash line, represent the layer boundaries associated with the mean momentum equation (Table I) corresponding to $\delta^+ = 1660$. Purple star position denotes where the conditional averages are computed in Figs. 4(b) and 5(a).

where N is the size of the ensemble, and the correlation coefficient is given by

$$R_{\tilde{v},\tilde{\kappa}_y} = \frac{r_{\tilde{v},\tilde{\kappa}_y}}{\sigma_{\tilde{v}}\sigma_{\tilde{\kappa}_y}}. \tag{12}$$

This correlation is nearly zero (slightly positive) close to the wall, but becomes negative elsewhere with a negative peak at $y^+ \approx 50$. Thus, except very near the wall, the wall-normal velocity $\tilde{v}$ and the associated curvature $\tilde{\kappa}_y$ are anticorrelated. Physically, this means that the wall-normal curvature is negative for the positive wall-normal velocity (flow away from the wall) and positive for the negative wall-normal velocity (wallward flow). Thus, relative to a quadrant decomposition involving $\tilde{v}$ and $\tilde{\kappa}_y$, the second and fourth quadrants are most heavily weighted.

To aid in understanding the features in Fig. 2(e), Fig. 3(a) presents an example of the streamline pattern closer to the wall with a valley and a peak denoted by the upward and downward arrows, respectively. The upward (*A*) and downward (*B*) double arrows show the inflection segments where sign changes happen between the concave up to concave down streamline shape. Note that the sign of the wall-normal curvature $\tilde{\kappa}_y$ is determined by the direction of a vector from the curve to its center of curvature. Here $\tilde{\kappa}_y$ is positive in the concave upward segment and negative in the concave downward segment. The arrows in Fig. 3(a) depict the center of curvature, which is essentially the inverse of curvature at the arrow starting point. From this, one therefore expects that at the positive peak in Fig. 2(e), streamlines of the orientation associated with the upward arrow of Fig. 3(a) are prevalent.

To clarify the directional sign changes of $\tilde{\kappa}_y$ along the streamline pattern of Fig. 3(a), all four possible cases are shown by the arrows and double arrows. The four cases arise from the positive and negative sign combinations of $\tilde{\kappa}_y$ and $\tilde{v}$. The region on the streamline adjacent to the upward arrow is a case where $\tilde{\kappa}_y$ is positive but v changes sign from negative to positive before and after the position of the arrow. Similarly, near the downward arrow $\tilde{\kappa}_y$ is negative but v changes sign from positive to negative before and after the arrow position. For the inflection region denoted by *A*, $\tilde{v}$ is positive but $\tilde{\kappa}_y$ changes sign from positive to negative. Similarly, for the inflection region denoted by *B*, $\tilde{v}$ is negative but $\tilde{\kappa}_y$ changes sign from negative to positive. Collectively, the cases just described characterize the conditions under which the sign of the $\tilde{v}$ and $\tilde{\kappa}_y$ product is determined.

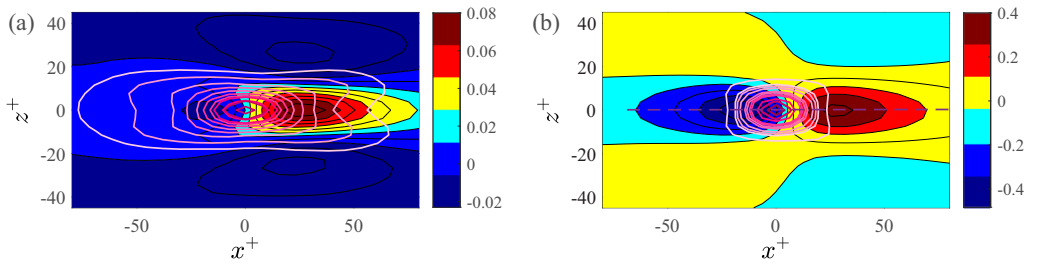

FIG. 4. (a) Data corresponding to $y^+ \approx 3$ for channel flow at $\delta^+ = 934$. The color contours are conditional average of $\tilde{v}^+$ corresponding to *positive* $\tilde{\kappa}_y^+$, whereas the (pink) lines are contour of $\tilde{\kappa}_y^+$ ranging from 0.5×10^{-3} to 4×10^{-3}, again conditioned on positive $\tilde{\kappa}_y^+$. (b) Same as (a); however, at $y^+ \approx 17$ for boundary layer flow at $\delta^+ = 2530$, where the range of the $\tilde{\kappa}_y^+$ (pink) contour lines are now 0.5×10^{-3} to 5×10^{-3}. Note that the color-bar range is not the same for the two figures owing to the different ranges associated with the color contours.

Figure 3(b) shows the correlation coefficient profiles of $\tilde{v}^+$ and $\tilde{\kappa}_y^+$. This plot reveals negative values except in layer I, where $\tilde{v}^+$ and $\tilde{\kappa}_y^+$ exhibit a weakly positive correlation. This plot also reveals an anticorrelation peak of $R_{\tilde{v},\tilde{\kappa}_y}$ at $y^+ \approx 17$, i.e., near the peak in the turbulence kinetic energy. Interestingly, the correlation function $r_{\tilde{v}^+,\tilde{\kappa}_y^+}$ shown in the inset plot of Fig. 2(e) shows only a mild negative value at the peak negative position of $R_{\tilde{v},\tilde{\kappa}_y}$. On the other hand, $r_{\tilde{v}^+,\tilde{\kappa}_y^+}$ shows a peak negative value at $y^+ \approx 50$. Thus, the shape of $R_{\tilde{v},\tilde{\kappa}_y}$, and $r_{\tilde{v}^+,\tilde{\kappa}_y^+}$ are distinctly different. Since $\sigma_{\tilde{\kappa}_y^+}$ is approximately constant [as discussed later relative to Fig. 6(c)], this shape difference of $R_{\tilde{v},\tilde{\kappa}_y}$ and $r_{\tilde{v}^+,\tilde{\kappa}_y^+}$ primarily comes from the significant variation in the fluctuating wall-normal velocity variance with y^+.

The distinctively negative $R_{\tilde{v},\tilde{\kappa}_y}$ values are examined further using conditional averages. The color contours in Fig. 4(a) are average $\tilde{v}$ conditioned on positive $\tilde{\kappa}_y^+$ values in the xz-plane at $y^+ \approx 3$ in the channel flow, i.e., at the positive peak of Fig. 2(e). Figure 4(b) shows (in color contours) $\tilde{v}^+$ conditionally averaged on positive $\tilde{\kappa}_y^+$ at the negative peak of $R_{\tilde{v},\tilde{\kappa}_y}$ at $y^+ \approx 17$ for the boundary layer flow. (Note that the statistical results for boundary layer and channel flow show similar behavior.) These averages of the positive $\tilde{\kappa}_y^+$ values are shown in Figs. 4(a) and 4(b) using (pink) lines, respectively. To better understand the location of the positive peak of $\tilde{\kappa}_y^+$ [deep pink lines in Figs. 4(a) and 4(b)] relative to the $\tilde{v}^+$ field, we have shown superimposed the color contours and the lines on the same figure. The anticorrelation property of $\tilde{v}^+$ and $\tilde{\kappa}_y^+$ nominally coincides with the condition where the pink contour of $\tilde{\kappa}_y^+$ overlaps with the peak negative region of $\tilde{v}^+$.

Close to the wall, $y^+ \approx 3$ [Fig. 4(a)], the positive wall normal curvature contours are nearly equally distributed between the positive and negative contours of v. This indicates nearly (and not exactly) equal probability of positive and negative v fluctuations for positive κ_y. To better understand this structure we draw reference to the upward arrow in Fig. 3(a) where the positive κ_y values correspond to both the positive and negative v values. At $y^+ \approx 17$ [Fig. 4(b)], positive κ_y^+ contours now reside more prevalently in the negative peak region of $\tilde{v}^+$. Thus, this case implies that for a situation like that near the upward arrow of Fig. 3(a), the positive κ_y values mostly correspond to a steep wallward trajectory, followed by a less steep trajectory away from the wall. This is also consistent with the correlation coefficient results in Fig. 3(b) where $\tilde{\kappa}_y^+$ and $\tilde{v}^+$ are anticorrelated except very near the wall.

To reinforce the anticorrelation result of Fig. 4(b), Fig. 5(a) shows the average of $\tilde{v}^+$ conditioned on negative $\tilde{\kappa}_y^+$ values at $y^+ \approx 17$. As expected, the green contours depicting the negative peak region of $\tilde{\kappa}_y^+$ reside more prevalently in the positive $\tilde{v}^+$ region. This case implies a situation like that near the downward arrow of Fig. 3(a) with the negative $\tilde{\kappa}_y$ values mostly corresponding to a steep

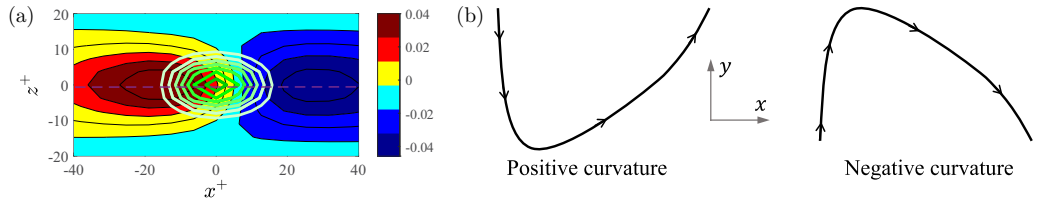

FIG. 5. (a) Same flow configuration ($y^+ \approx 17$ for boundary layer flow at $\delta^+ = 2530$) as Fig. 4(b), except now conditioned on *negative* $\tilde{\kappa}_y^+$. The (green) contour lines denote the negative values of $\tilde{\kappa}_y^+$ ranging from -3.5×10^{-4} to 0. (b) Sketch of representative streamlines with positive and negative curvatures, respectively, illustrating the conditional Figs. 4(b) and 5(a).

trajectory away from the wall, followed by a shallower wallward trajectory. Figure 5(b) contains representative features associated with a streamline pattern consistent with the average behaviors along the dashed centerline of Figs. 4(b) and 5(a). Here the anticorrelation case of Fig. 4(b) (positive $\tilde{\kappa}_y^+$ and negative $\tilde{v}^+$) corresponds to the streamline pattern below the dashed line of Fig. 5(b), while the anticorrelation case of Fig. 5(a) (negative $\tilde{\kappa}_y^+$ and positive $\tilde{v}^+$) corresponds to the streamline pattern above the dashed line.

Thus, to summarize, the peak positive value of $\overline{\tilde{\kappa}_y^+}$ in Fig. 2(e) at $y^+ \approx 3$ corresponds approximately to the concave upward peak region on a streamline pattern like that of the streamline segment shown in Fig. 5(b) with the positive curvature. This representative streamline is constructed from the conditional plot in Fig 4(b). The streamline depicts a wallward v and with the center of curvature pointing away from the wall. Here the concave upward shape of this streamline (associated with positive κ_y) occurs in concert with a wallward v followed by a weaker v flow away from the wall. Therefore, the positive peak of $\overline{\tilde{\kappa}_y^+}$ in Fig. 2(e) is largely associated with wallward v velocities. Similarly, the negative $\overline{\tilde{\kappa}_y^+}$ in Fig. 2(e) at $y^+ \approx 17$ corresponding to strong negative $R_{\tilde{v},\tilde{\kappa}_y}$ is related to the strong positive v velocities followed by a weaker v flow towards the wall. This is akin to the streamline segment in Fig. 5(b) with the negative curvature, which is representing the conditional plot in Fig. 5(a).

Interestingly, it might seem that the connection between $\tilde{\kappa}_y$ and $\tilde{v}$ might be related to the well-known "sweep" and "ejection" events in the boundary layer. Sweep/ejections are typically associated with the fluctuating velocity joint pdf of (u, v), and here our discussion relates to total velocities. Nevertheless, we did compute the joint pdf of the total velocities $(\tilde{u}, \tilde{v})$, which has an area of each 0.5 for both positive and negative $\tilde{v}$ since the mean $\tilde{v}$ is zero (for channel and close to zero for BL). Importantly, at $y^+ = 17$, when we condition the joint pdf of $(\tilde{u}, \tilde{v})$ on $\tilde{\kappa}_y > 0$, we find 0.53 as the area for negative $\tilde{v}$ rather than 0.5, and a consistent 0.47 for positive $\tilde{v}$. Also, when conditioned on $\tilde{\kappa}_y < 0$, we find the area under positive $\tilde{v}$ as 0.57 and 0.43 under negative $\tilde{v}$. These results strengthen our previous assertion that negative $\tilde{\kappa}_y$ is associated with positive $\tilde{v}$, and vice versa. A similar, however, less pronounced result is also observed at $y^+ = 3$.

3. Standard deviation versus mean curvature

The ratio of the mean curvature to the standard deviation provides an indication of the relative importance of the fluctuations. Figure 6 presents the ratios of the mean curvatures to their standard deviations. The vertical dashed lines are again the momentum balance layer boundaries at $\delta^+ \approx 1660$ for the boundary layer flow. Figure 6(a) shows the curvature magnitude ratio. This ratio has its lowest value near the wall, then increases with distance from the wall, and reaches a peak value near the onset of the inertial region, i.e., near the outer edge of layer III. After that, it attains a plateau near unity in the log layer, and then rapidly decreases in the outer region. Thus, the curvature variance is larger than the mean out to a position near the outer edge of layer II. From layer III, the variance

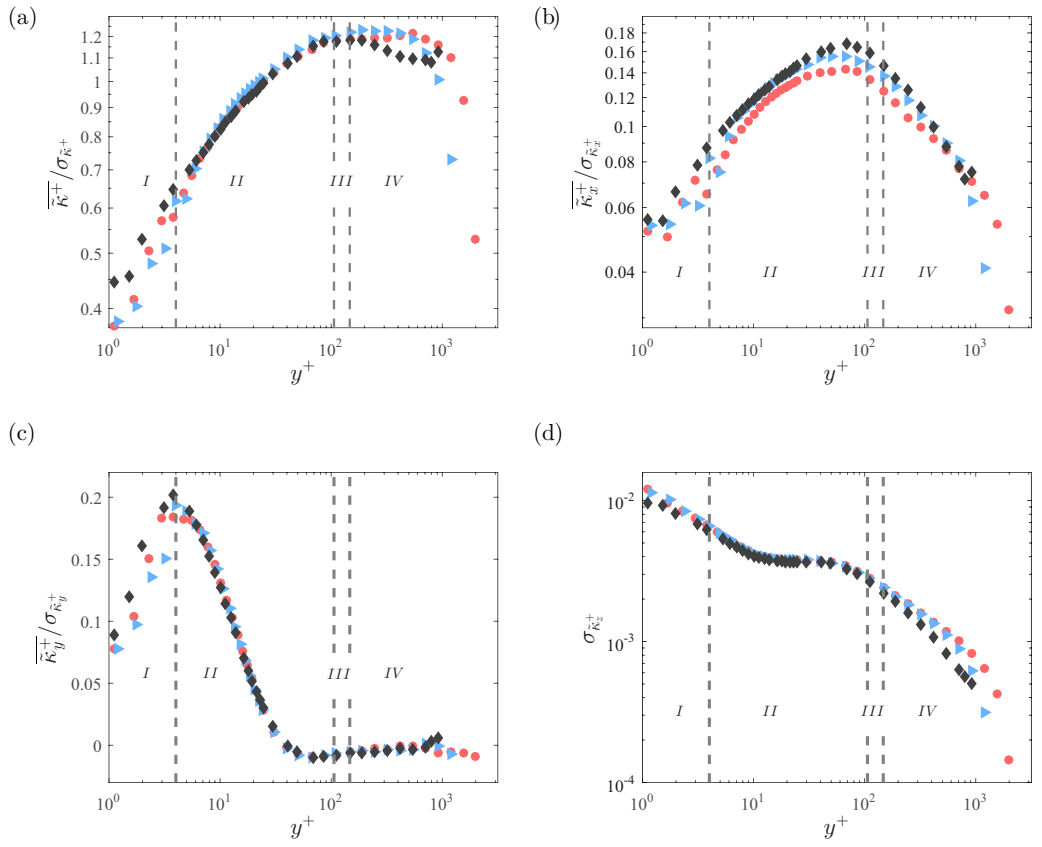

FIG. 6. The ratio of the mean and standard deviation of the curvatures in case of the boundary layer (colored) (Red circle, for $\delta^+ \approx 2530$ and blue triangle, for $\delta^+ \approx 1660$) and the channel flow (black diamond, for $\delta^+ \approx 934$). The vertical gray dash line, represent the layer boundaries associated with the mean momentum equation (Table I) corresponding to $\delta^+ = 1660$. (a) Curvature magnitude ratio; (b) streamwise curvature ratio; (c) wall-normal curvature ratio and; (d) standard deviation of curvature in the spanwise direction.

becomes slightly smaller than the mean until the center of layer IV, after which it becomes larger than the mean out to $y^+ \simeq \delta$.

Figure 6(b) shows the ratio of the mean to the standard deviation for the streamwise curvature component. Here there is an increasing trend up to a peak near the outer edge of layer II (due to likely three-dimensionalization of the flow), followed by a decrease across the log layer. This indicates that the minimum average fluctuation relative to the mean occurs near the outer edge of layer II. The ratio for the wall-normal curvature, Fig. 6(c) behaves in the similar trend as $\overline{\tilde{\kappa}_y^+}$ in Fig. 2(e). This plot also shows a positive peak at the same wall location as the positive peak of Fig. 2(e). After the peak value, it decreases rapidly and remains constant from the outer edge of layer II outward. When combined with Fig. 2(e), this figure reveals that the variance of κ_y remains approximately constant across the flow.

Figure 6(d) presents the standard deviation of $\tilde{\kappa}_z^+$, rather than the ratio of the mean to the standard deviation because the mean value $\overline{\tilde{\kappa}_z^+} \approx 0$ everywhere [cf. Fig. 2(f)]. This figure shows a decreasing magnitude with distance from the wall similar to $\overline{\tilde{\kappa}^+}$ in Fig. 2(a). All the ratios in Fig. 6 show that the maximum variances relative to the mean respectively occur near $y^+ \simeq 0$, and near $y^+ \simeq \delta$.

The statistical profiles in Figs. 2 and 6 are derived from the total velocity field. These statistics indicate that the streamlines with large curvature values are generally concentrated closer to the wall. The distribution of curvatures can, however, be analyzed in greater depth by examining probability density functions at locations of interest. The next section covers the properties of curvature pdfs as derived from both the total and fluctuating velocity fields at the positions denoted by the violet stars in Fig. 2.

B. Curvature probability density functions

The distribution of curvature values at a given wall-normal location contains information about the scales of motion at that location. For isotropic flow, Schaefer [7] found that for a range of large curvatures, the pdf of κ exhibits tails having a power-law slope of -4. This can be derived under the assumptions noted in the Introduction. Physically, large values of curvature are associated with small length scales of the turbulent flow and vice versa. When these small length scales are of the order of the Kolmogorov length scale η, they lose connection to the energetic turbulent motions. The exponent of -4 is the scaling associated with these extreme curvature values, and the results of Schaefer [7] support this description. Streamlines approaching a stagnation region are sharply deflected. From this Schaefer describes the expectation that the stagnation points essentially cause these extreme values of curvature. These findings are reinforced and clarified for wall-turbulence in the present joint pdf results.

Figure 7 presents the pdf of curvature magnitudes at the wall-normal locations identified in Fig. 2. Here the pdf results are computed using the $\delta^+ = 2530$ boundary layer DNS. The left side plots of Fig. 7 are computed using the total velocity field, while the right side results are calculated using the fluctuating velocity field. The solid blue line represents a power law with an exponent of -4. Figure 7(a) shows the pdfs of curvature magnitude ($P(|\tilde{\kappa}^+|)$), where different symbols are for different y^+. Here the -4 scaling is apparent only close to the wall. For fluctuating velocity fields ($P(|\kappa^+|)$) in Fig. 7(b), however, κ^{-4} scaling is more apparent away from the wall. It is interesting to note that the mean value of κ^+ is not far away from the κ^+ value beyond which the -4 scaling seems to hold.

Figures 7(c) and 7(d) show streamwise curvature magnitude pdfs. Here the $P(\tilde{\kappa}_x^+)$ for both total and fluctuating velocity fields are qualitatively similar with different magnitudes and exhibit -4 scaling for positions away from the wall. Distinct from this, the wall-normal curvature pdfs in Figs. 7(e) and 7(f) for the total and fluctuating streamlines are different. For the total velocity field, the $P(|\tilde{\kappa}_y^+|)$ profiles fall on top of each other for different wall-normal locations, and they do not follow $\tilde{\kappa}_y^{-4}$ scaling except possibly for a small region near the wall. On the other hand, in Fig. 7(f) $P(|\kappa_y^+|)$ varies with wall-positions and follows κ_y^{-4} scaling at positions away from the wall. Here it is important to recognize that if κ_y were to depend only on v, then the calculations using the total and fluctuating cases would be the same, since the mean V is zero (for channel flow). This is not the case, however, as κ_y does not depend on only v but also on the other velocity components. The different behavior of curvature pdfs for total and fluctuating flow fields is not unexpected given the differences we observed in the streamline patterns of total and fluctuating velocity fields in Fig. 1.

A number of results in Fig. 7 indicate that the first appearance of -4 scaling depends on y^+. To examine the onset of this behavior, Fig. 8 presents the pdfs multiplied by the associated curvatures raised to the fourth power at more wall-positions than considered in Fig. 7. The pink stars denote the approximate onset of -4 scaling and are located by visual inspection. Figure 8(a) shows that κ approximately follows κ^{-4} scaling over a significant κ range starting around $y^+ = 20$ outward for the fluctuating velocity field. The κ_y^{-4} scaling in Fig. 8(b) also starts near $y^+ = 20$. For the total velocity field in Fig. 8(c), however, the $\tilde{\kappa}_y^{-4}$ scaling does not convincingly appear anywhere. Here the most important observation is that with increasing y^+ a greater portion of the κ and κ_y pdfs adhere to -4 scaling. This correlates with the decreasing influence of viscous effects with increasing y^+.

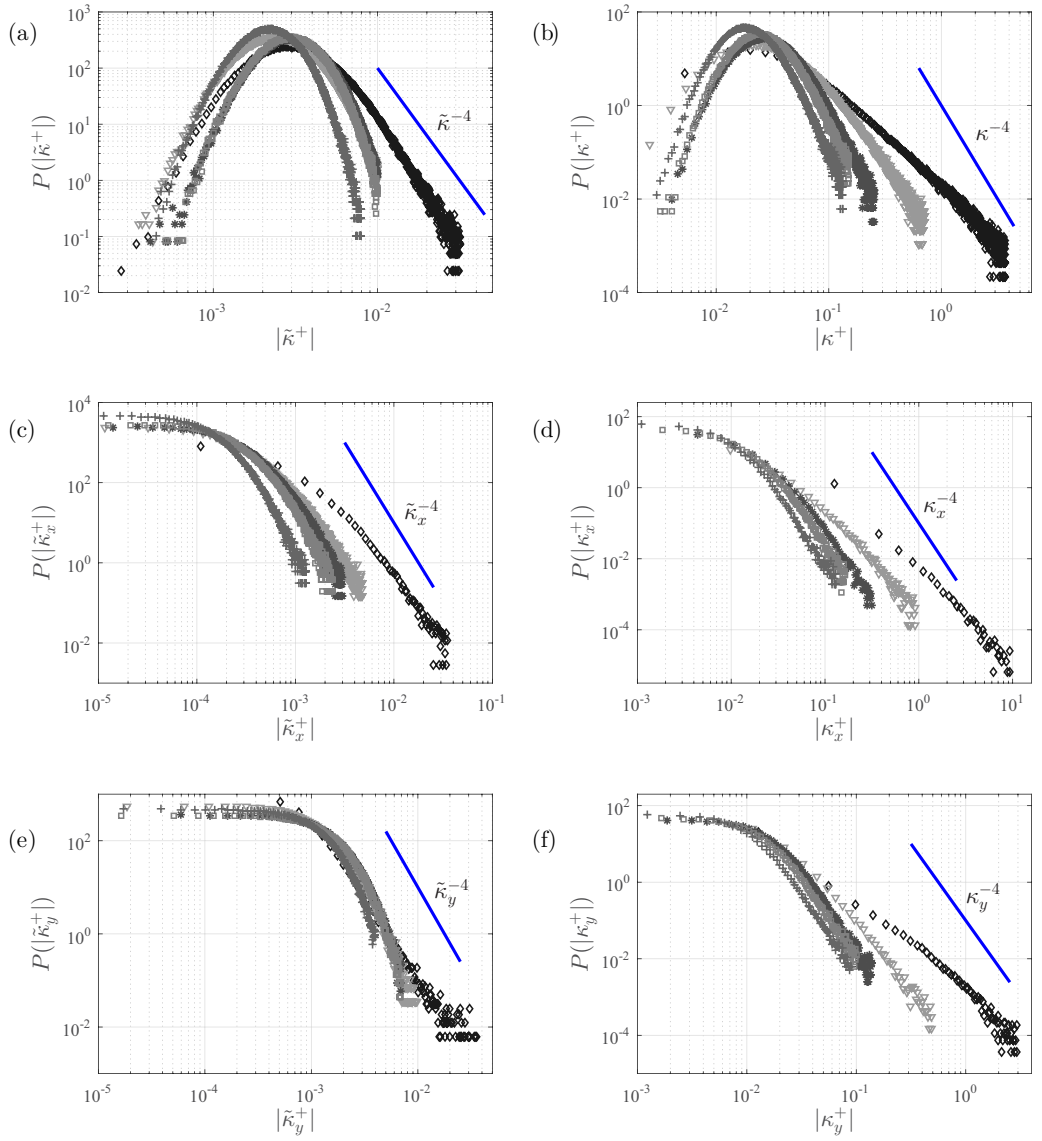

FIG. 7. Probability density function of the curvature magnitude and curvature components for boundary layer flow at $\delta^+ = 2530$ at varying wall-normal locations; diamond, $y^+ = 3$; triangle, $y^+ = 14$, star, $y^+ = 40$, square, $y^+ = 67$; plus, $y^+ = 174$. (a) Probability of the curvature magnitude computed from the instantaneous streamlines pattern; (b) probability of the curvature magnitude for the fluctuating streamlines pattern; (c) probability of the streamwise curvature for the instantaneous streamlines pattern; (d) probability of the streamwise curvature for the fluctuating streamlines pattern; (e) probability of the wall-normal curvature for the instantaneous streamlines pattern; (f) probability of the wall-normal curvature determined from the fluctuating streamlines pattern.

The κ^{-4} scaling is related to the fraction of the pdf associated with small-scale motions. The onset of this scaling at different wall locations may correspond to features associated with the influence of the stagnation regions as described in the analysis of Schaefer [7].

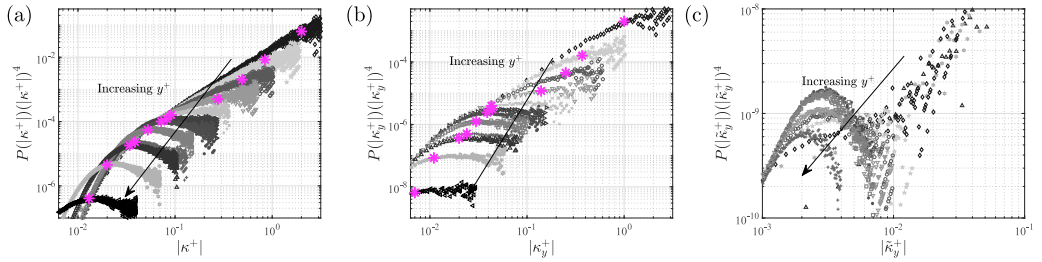

FIG. 8. Compensated curvature pdfs for boundary layer flow at $\delta^+ = 2530$. (a) κ^{-4} scaling for fluctuating velocity field; (b) κ_y^{-4} scaling for velocity fluctuating field; (c) $\tilde{\kappa}_y^{-4}$ scaling for total velocity field. The y locations start at $y^+ = 3$ from the top in (a) and (b) and decrease downwards. Pink stars denote the estimated onset of κ^{-4} scaling.

Figure 9(a) provides insights that connect the onset of -4 scaling with the stagnation point studies by Vassilicos and group described in the Introduction. These studies demonstrate that the dissipation rate depends linearly on the density of the stagnation points in the logarithmic layer [23]. Here we focus on the curvature statistics obtained from the fluctuating velocity field because as observed in Fig. 8, the κ^{-4} scaling is unambiguously present only for fluctuating fields. Furthermore, this lends a more straightforward comparison with the results of other researchers from isotropic turbulence mentioned in the Introduction.

Figure 9(a) shows the onset of -4 scaling κ_0 for fluctuating velocity field [denoted by the pink stars in Fig. 8(a)] along with the inverse of the Kolmogorov scale. Here η^+ has been computed based on both the isotropic approximation and the actual viscous dissipation rate. Namely, η^+ is calculated using $\epsilon = 15\nu\overline{(\partial u_1/\partial x_1)^2}$ and η_ϵ is calculated using $\epsilon = 2\nu\overline{s_{ij}s_{ij}}$. The profile characterizing the onset of -4 scaling shows a decreasing trend relative to y^+, i.e., the length scales increase. Although the trends of both $1/\eta$ and κ_0 w.r.t y^+ look similar, they are offset by a factor of 10 beyond $y^+ \approx 50$, indicating that the length scales below which we expect κ^{-4} scaling is $\approx 10\eta$. We note that this is

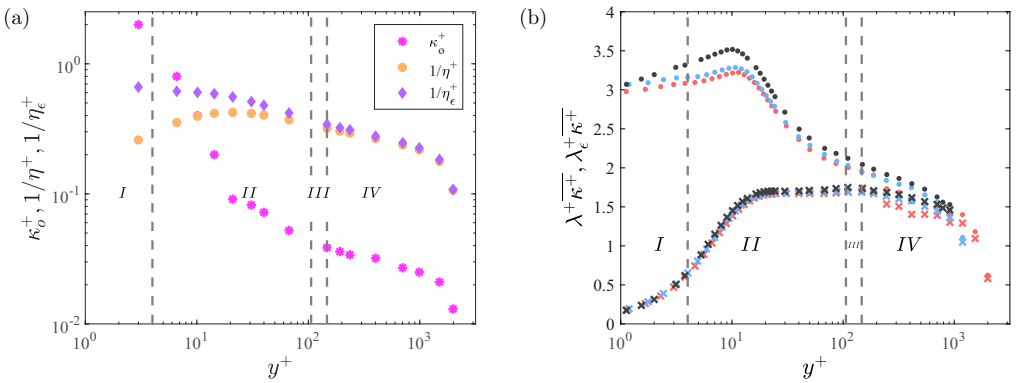

FIG. 9. (a) κ^+ (curvature magnitude for fluctuating streamlines) values at which κ^{-4} behavior is first observed in the κ^+ pdf plot [Fig. 7(b) or Fig. 8(a)] versus y^+; i.e., the onset of κ^{-4} behavior, denoted by κ_o^+, as a function of y^+. Comparison is made between κ_o^{-4} and the inverse of Kolmogorov length scale $(1/\eta^+)$, where η^+ is computed from the total strain-rate η_ϵ^+ and using the isotropic assumption. (b) Ratio of λ^+ [using the definitions from Eqs. (9) (dot symbols) and (10) (cross symbols)] and the inverse of curvature magnitude in case of the boundary layers (red symbols for $\delta^+ \approx 2530$; blue symbols for $\delta^+ \approx 1660$) and the channel flow (black symbols for $\delta^+ \approx 934$). The vertical gray dash lines indicate the position of the momentum balance layer boundaries associated with $\delta^+ = 1660$ (Table I).

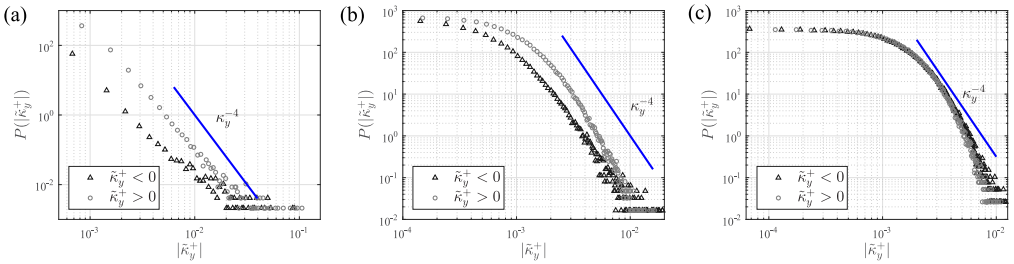

FIG. 10. PDF for positive and negative values of $\tilde{\kappa}_y^+$ at (a) the positive peak position of Fig. 2(e) i.e., at $y^+ = 3$, (b) at $y^+ = 10$, and (c) at $y^+ = 30$.

approximately $\lambda/3$. These estimates are consistent with the pdfs presented in Fig. 8(a), where the κ^{-4} scaling is observed at length scales larger than η [by reading $1/\eta^+$ from Fig. 9(a) and comparing with the abscissa of Fig. 8(a)].

Figure 9(b) shows the ratio of the Taylor microscale to the mean radius of curvature ($1/\overline{\kappa^+}$) at different wall-normal locations. Here the two different symbols represent two different definitions of λ, where dot symbols use Eq. (9) and the cross symbols use Eq. (10). As discussed before, the isotropic formula is not a good approximation in the near-wall region. This is reflected by the deviations up to $y^+ \simeq 50$. The cross symbol profiles (using the total dissipation rate) indicate that the radius of curvature is greater than the intermediate scale λ^+ in layer I. From layer II, the radius of curvature becomes less than the Taylor microscale. This ratio shows a peak near the peak in the turbulent kinetic energy, i.e., near $y^+ \simeq 15$. For greater y^+, the ratio decreases gradually outward. Here the curvature radius remains less than the Taylor microscale, although of the same order of magnitude. Beyond $y^+ \simeq 50$, the radius of curvature varies approximately in proportion to the Taylor microscale. On the inertial domain, the onset of -4 scaling and the inverse of Kolmogorov scale of Fig. 9(a) and the ratio of Fig. 9(b) exhibit power-law dependencies on y^+ that are consistent with the classical scaling of η and λ.

Collectively, the above results draw interesting connections between the studies of Klewicki [11], Vassilicos *et al.* [23], [8], and Schaefer [7]. As illustrated in Fig. 2(c), Klewicki [11] showed that beyond $y^+ \simeq 50$ the mechanism of vorticity stretching significantly weakens and vorticity advection leads to the spatial dispersion of vorticity—a mechanism that increasingly dominates with increasing y^+. In the inertial domain, Fig. 9(a) shows that κ_o^+ (where -4 power-law scaling begins) varies in a similar trend with a power law to the inverse of the $\approx 10\eta$, whereas in accord with Schaefer [7], the radius of curvature varies in proportion to λ as shown in Fig. 9(b). On the same domain, the density of stagnation points decreases like $1/y^+$ [8]. This is not inconsistent with the onset of -4 scaling [Fig. 9(a)] that also decreases with y^+ over the same domain. The nonproportionalities of $1/\kappa_o^+ \propto 10\eta^+$ and $1/\overline{\kappa^+} \propto \lambda^+$ before $y^+ \simeq 50$ arise from the overall effect of the wall. Rationally, these can stem from either viscous or wall-blocking effects. To better understand the wall-blocking limit, the pdf of wall-normal curvature is now analyzed.

Viscous effects are expected to affect the positive and negative $\tilde{\kappa}_y^+$ values proportionally whereas wall-blocking effect will be reflected in an asymmetry in the $\tilde{\kappa}_y^+$ pdf about the zero value. Figures 10(a)–10(c) present pdfs for the positive and rectified negative values of $\tilde{\kappa}_y^+$ at $y^+ = 3$, $y^+ = 10$ and $y^+ = 30$, respectively. For isotropic flow, the behavior of the pdf tail is symmetric about its mean. Figures 10(a) and 10(b) reveal that the profiles for the positive and negative values of $\tilde{\kappa}_y^+$ are different near the wall. On the other hand, Fig. 10(c) reveals that by $y^+ = 30$, the $\tilde{\kappa}_y^+$ pdf becomes nearly symmetric. These results suggest a wall-blocking effect for $y^+ \lesssim 30$. The observed asymmetry of the pdf $y^+ < 30$ in Fig. 10 cannot, however, be wholly attributed to viscous effect. That is, if this were the case, then all the plots of Fig. 10 (within layer II where the viscous force is leading order) would show similar behavior. Thus, Figs. 10(a) and 10(b) are surmised to show

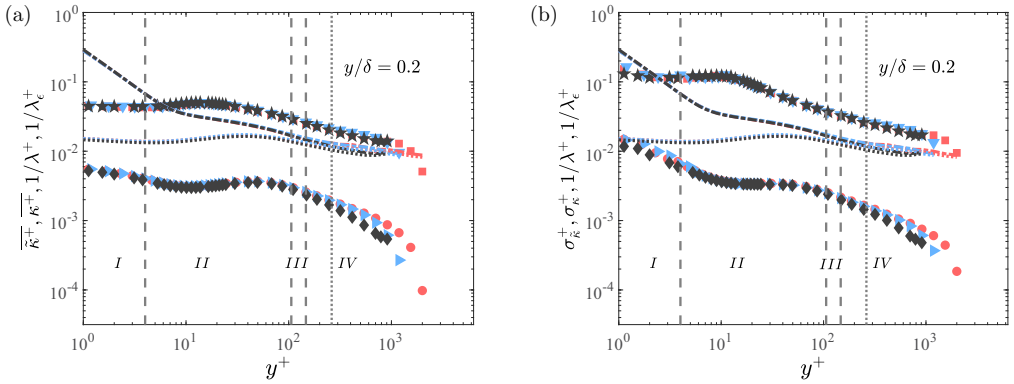

FIG. 11. Statistics of curvature in case of the boundary layer (colored) (Red circle, for $\delta^+ \approx 2530$ and blue triangle, for $\delta^+ \approx 1660$) and the channel flow (black diamond, for $\delta^+ \approx 934$) compared with the inverse of Taylor microscale [dot symbol, using Eq. (9) and dash dot symbol, using Eq. (10)]. Vertical gray dash lines, represent the layer boundaries associated with the mean momentum equation (Table I) corresponding to $\delta^+ = 1660$. (a) Mean curvature statistics for total (lower curves) and fluctuating field (upper curves); (b) standard deviation of curvature for total (lower curves) and fluctuating field (upper curves).

profiles different from the symmetric one at $y^+ = 30$ owing to a wall-blocking effect. From this, we further surmise that between $30 \lesssim y^+ \lesssim 50$, the nonproportional results of Figs. 9(a) and 9(b) most likely occur because of viscous effects.

Although in Fig. 2(a) we presented the mean curvature from total velocity field $\overline{\tilde{\kappa}}$, and in Fig. 9(b) the mean curvature data from fluctuating velocity field $\overline{\kappa}$, given that in wall-turbulence the two curvatures differ significantly, we find it worth making a direct comparison.

We therefore replot $\overline{\tilde{\kappa}}$ and $\overline{\kappa}$ in Fig. 11(a) and compare them with the inverse of the Taylor microscale. Both $\overline{\tilde{\kappa}}$ and $\overline{\kappa}$ decrease with y^+ at a similar rate (especially in the inertial region). Furthermore, not surprisingly, the mean curvature from the total velocity field $\overline{\tilde{\kappa}}$ is smaller than $\overline{\kappa}$, and they differ by a factor of about 10. In Fig. 11(b) we compare the standard deviation of the curvature evaluated from the total as well as the fluctuating field, $\sigma_{\tilde{\kappa}}^+$ and σ_κ^+ respectively, with λ. We find that not only the mean, but rather the standard deviation of the curvature from the fluctuating field is also closer to the Taylor microscale compared to those calculated from the total field. This is similar to what other studies (e.g., [7]) have found under isotropic flow conditions, where the mean flow does not exist, or from uniform shear flows where the effect of mean flow is negligible.

C. Torsion

Torsion (τ) is a measure of the twisting of the streamlines out of a reference plane of motion. Similar to curvature, torsion is a length scale associated with the shape and size of the potential twisting of a streamline where the inverse of torsion can be conceptualized as a radius of torsion. Torsion is positive or negative based on whether the streamline is moving with or counter to the binormal vector (cf. Sec. II B). Thus, positive and negative torsions are related to the out of plane motion rather than moving towards or moving away from the wall. For example, the torsion is positive for right-hand helix moving away from the wall but torsion is negative while also moving away from the wall for left-hand helix, and vice versa.

Figure 12(a) presents the mean torsion ($\overline{\tilde{\tau}^+}$) versus y^+. Here $\overline{\tilde{\tau}^+}$ values are essentially zero (possibly slightly negative) for all y^+. The nearly zero values for the $\overline{\tilde{\tau}^+}$ is basically a fraction of the symmetry of the instantaneous torsion pdf. If we consider the right-hand helix rule for the

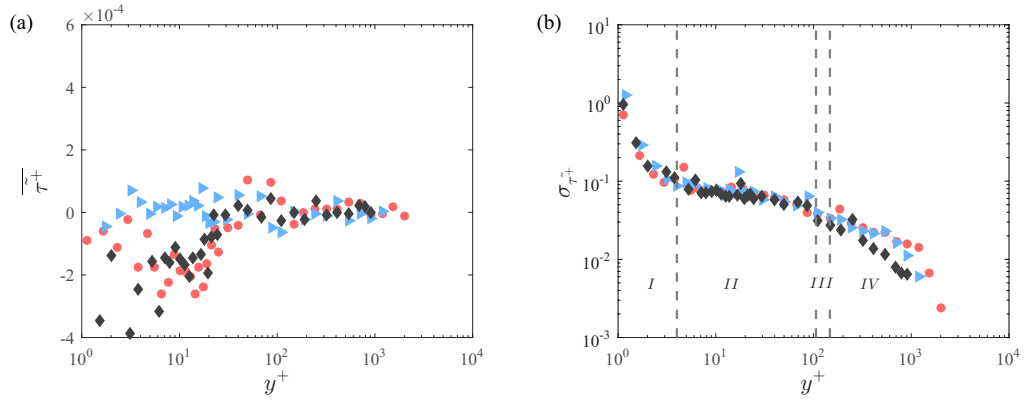

FIG. 12. Torsion statistics of curvature in case of the boundary layer (colored) (Red circle, for $\delta^+ \approx 2530$ and blue triangle, for $\delta^+ \approx 1660$) and the channel flow (black diamond, for $\delta^+ \approx 934$). The vertical gray dash lines, represent the layer boundaries associated with the mean momentum equation (Table I) corresponding to $\delta^+ = 1660$. (a) Mean; (b) standard deviation.

streamlines and employ the Frenet-Serret apparatus (Sec. II B), the negative torsion reveals that the streamlines are moving opposite to the binormal vector direction.

Figure 12(b) shows the standard deviation of torsion versus y^+. These data reach their maximum at a location near $y^+ = 1$ and then decreases with distance from the wall. This indicates that streamline patterns that twist out of the x-z-plane are more prevalent in the near-wall region. Physically, this is consistent with the rapid three-dimensionalization of the velocity field from the wall outward.

We now compare the relative strength of bending and twisting of streamlines by examining the ratio of the curvature to the torsion across the flow. Figure 13(a) shows this ratio using the total velocity field at different wall-normal locations. The ratio has a maximum value close to the wall and then shows an approximately power-law decay across layer II. Beyond $y^+ \simeq 100$ to the outer edge of the inertial layer, the ratio is nominally constant. Figure 13(b) using the fluctuating velocity field also presents a similar decreasing behavior up to the center of layer II and then attains an

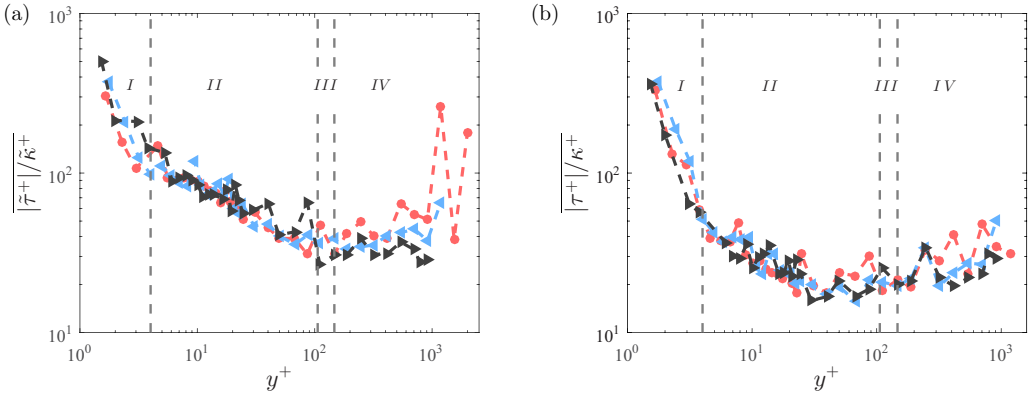

FIG. 13. Ratio of τ and κ for (a) the total velocity field and (b) the fluctuating velocity field in case of the boundary layer (colored) (Red circle, for $\delta^+ \approx 2530$ and blue triangle, for $\delta^+ \approx 1660$) and the channel flow (black diamond, for $\delta^+ \approx 934$). The vertical gray dash lines, represent the layer boundaries associated with the mean momentum equation (Table I) corresponding to $\delta^+ = 1660$.

approximately constant much greater than one. Thus, this ratio reveals intense twisting motion than bending over the flow domain.

D. Joint probability density function

In this section we consider the fluctuating streamline pattern, with special attention on the streamline curvature behavior in stagnation regions $(u, v, w) \cong 0$. Figure 14 presents the joint probability density function of the fluctuating velocity magnitude $|V| = \sqrt{u^2 + v^2 + w^2}$, and the inverse of fluctuating curvature magnitude, i.e., the radius of curvature, at four wall-positions residing within the four layers noted in Table I. Figure 14(a) shows the joint probability contour of $|V^+|$ and $1/\kappa^+$ in the viscous sublayer. Here the contour lines corresponding to small radius of curvature $(1/\kappa^+)$ is weighted towards the minimum value of the velocity magnitude $(|V^+|) \approx 0$). Although indirect, this supports the notion that curvature values are maximal in stagnation regions $(|V^+|) \approx 0$). This feature remains prevalent with distance from the wall as shown in Figs. 14(b)–14(d) in layers II–IV, respectively. This result nominally agrees with the conclusion of Schaefer [7], that extreme curvature values occur owing to sharply deflected streamlines in the vicinity of stagnation points.

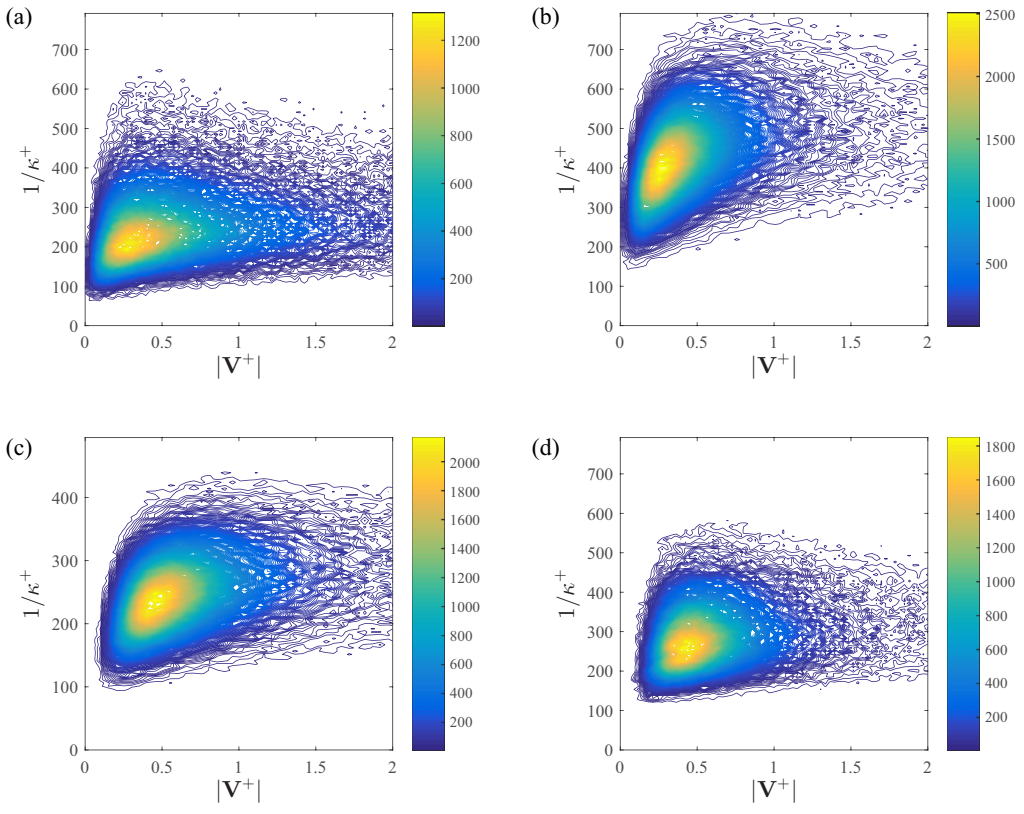

FIG. 14. Joint pdf of the fluctuating velocity magnitude with the inverse of curvature magnitude for fluctuating streamlines pattern in case of the Channel flow at (a) $y^+ = 3$, (b) $y^+ = 30$, (c) $y^+ = 63$, and (d) $y^+ = 911$.

1. Joint PDF of the curvature components

The orientations of the streamlines determines the curvature components. To understand the geometric characteristics of the streamlines in each layer of Table I, jpdfs of all three combinations for fluctuating κ_x, κ_y and κ_z were examined. For $y^+ \lesssim 30$, the jpdfs show distortion from symmetry due to the presence of the wall. This is reflected by noncircular contours. With increasing distance, however, the joint pdfs of (κ_x^+, κ_z^+) as well as (κ_y^+, κ_z^+) exhibit essentially circular pdfs centered about zero, yielding the correlation coefficient of about 0.01 or less (not shown here).

Very close to the wall, the joint distribution of κ_x^+, κ_y^+ in Fig. 15(a) shows a distorted shape concentrating in the second quadrant. This distortion most likely arises due to a combination of the viscous shear effect on κ_x^+ and a wall-blocking effect on κ_y^+, as discussed earlier. Figure 15(b) in layer II also shows a somewhat distorted pdf that is weighted in the first and second quadrant. In layer III, Fig. 15(c) presents that the pdf is weighted in the first and second quadrant with the correlation coefficient, $R_{\kappa_x,\kappa_y} \cong -0.1$. Beyond this position and up to the centerline of the channel flow, e.g., Fig. 15(d), the pdfs exhibit essentially circular contours centered about zero with $R_{\kappa_x,\kappa_y} \cong 0$. Here we note that κ_x^+ pdf is more distorted (or symmetric) than κ_y^+ pdf before layer III. From layer III, the distortion of κ_x^+ presumably owing to the shear diminishes. Within this region the transfer of the mean shear into fluctuating vorticity also diminishes [11]. This diminishing mean shear effect terminates near $y^+ = 50$, where the vorticity intensities are all nearly equal in magnitude [11]. These results reinforce those surmised from Fig. 10 that the wall-blocking effect is most important for $y^+ \lesssim 30$, while the shear effect extends to $y^+ \simeq 50$.

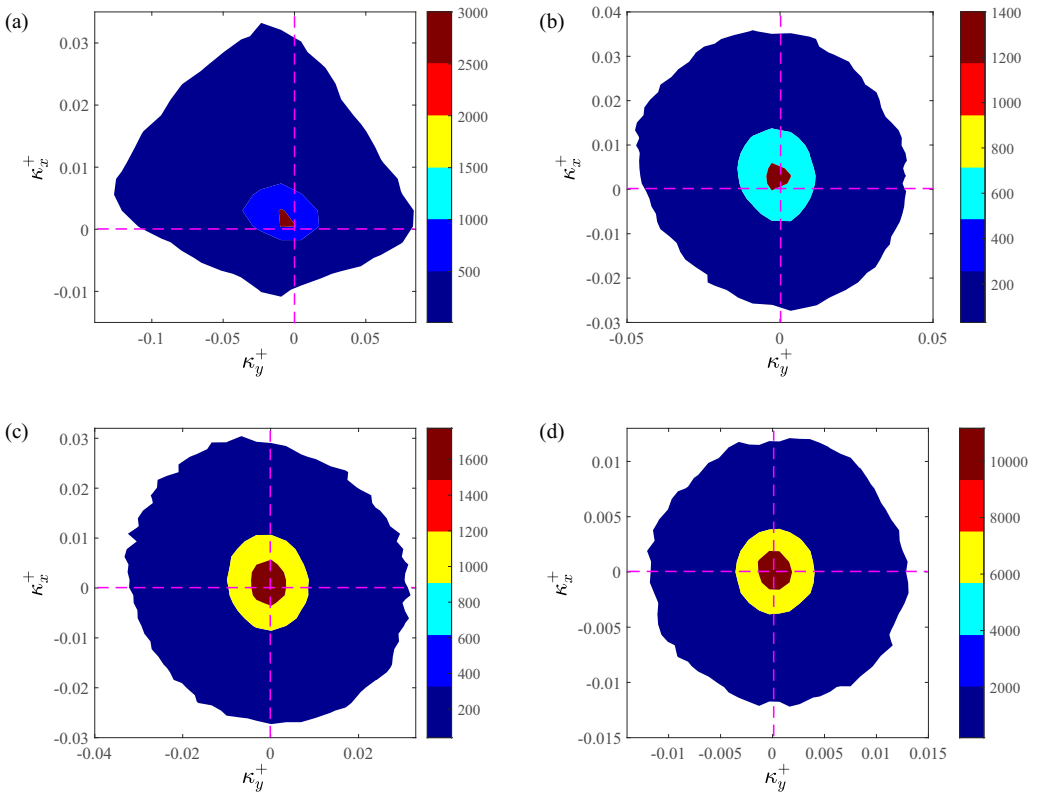

FIG. 15. (a) Joint pdf of the streamwise curvature component with wall-normal curvature component for fluctuating streamlines pattern in case of the Channel flow at (a) $y^+ = 3$, (b) $y^+ = 30$, (c) $y^+ = 63$, and (d) $y^+ = 911$.

IV. SUMMARY AND CONCLUSIONS

The present study describes statistical properties of the streamline curvature and torsion in turbulent wall-flows. The streamlines of the flows were calculated from available DNS [33,34] and used a fourth-order Runge-Kutta method. The Frenet-Serret formulas from differential geometry were used to evaluate κ and τ. Curvature is calculated using the tangent vectors and the arc length of the corresponding streamline curve. Torsion is evaluated using central difference formulas for the derivative terms in the definitional equation of τ. Although statistics of curvature and torsion for both boundary layer and channel flows are evaluated, we find that these statistics are broadly similar across the two flow types and the range of Reynolds number investigated. The fact that streamline geometry statistics scale mostly with small-scale flow features such as η or λ might be the likely reason that we do not observe significant differences across flow types. The reason for minimal Re-dependence could further be accentuated by the limited Re-range used in our study. Therefore, the salient features of the streamline geometry are presented without particular emphasis on the flow type or Re.

We find that curvature statistics show varying behavior close to the wall, and between $y^+ \simeq 17$ (the peak location of the turbulent kinetic energy) and $y^+ \simeq 50$. At $y^+ \simeq 50$, vorticity advection becomes an increasingly prevalent mechanism leading to the spatial dispersion of vorticity that increasingly dominates with increasing y^+ [11]. In the classical log layer, the radius of curvature exhibits a power-law variation that varies approximately like the Taylor microscale. The maximum variance of curvature corresponding to the mean occurs close to the wall and close to the channel centerline. This is revealed using the ratio of mean curvature to its standard deviation.

An interesting result from the mean statistics is that $\overline{\tilde{\kappa}_y^+}$ exhibits a positive peak close to the wall. To understand this, the correlation coefficient of $\tilde{v}^+$ and $\tilde{\kappa}_y^+$ and the conditional average of $\tilde{v}^+$ field corresponding to positive $\tilde{\kappa}_y^+$ were computed. The results show an anticorrelation between $\tilde{v}^+$ and $\tilde{\kappa}_y^+$ except close to the wall. These results support that the positive $\overline{\tilde{\kappa}_y^+}$ peak is associated with a strong negative $\tilde{v}^+$ followed by a weaker positive $\tilde{v}^+$. In other words, the positive peak near the wall is related to strong wallward flowing streamlines.

The pdfs of the curvature magnitude and the curvature components with an exponent of -4 scaling have been shown for a varying degree in both total and fluctuating velocity fields, but more prominent for curvature from fluctuating velocity field. From these analyses, it is apparent that κ^{-4} scaling is predominant at increasing distances from the wall. The -4 scaling is relevant to describing the large curvature values in stagnation regions [7] (see Fig. 16). The curvature value at the onset of this scaling κ_o is comparable to the inverse of $\approx 10\eta$ at different wall positions beyond $y^+ \approx 50$. Here both κ_o and η are found to show a power-law decrease with y^+ in the inertial domain (logarithmic layer). This is not inconsistent with the decreasing number density of stagnation points with y^+ in the inertial layer [8]. The present results indicate that, the onset of -4 scaling varies in a similar trend with the Kolmogorov scale and the mean radius of curvature varies proportionally with the Taylor microscale on the inertial layer. The nonproportional results for $y^+ \lesssim 50$ arise from the wall-blocking effect within $y^+ \approx 30$, and from the viscous effect within that extends to near $y^+ = 50$. This finding is reinforced by analyzing the positive and negative pdf profiles of the wall-normal curvature, and the joint pdfs of curvature components. The properties of the out of plane motion of the streamlines have been shown by the mean and the standard deviation statistics of torsion. The ratio of torsion to the curvature reveals that the out of plane pattern is smaller scale than the in-plane pattern for both total and fluctuating streamlines.

The joint pdf results describe the streamline pattern and behavior in stagnation regions is depicted schematically in Fig. 16. Here the high curvature values are associated with streamlines that come near to an advecting stagnation region, where they are sharply deflected. On the inertial domain, the number density of stagnation points decays like $1/y^+$ [8]. The onset of -4 scaling of curvature is proportional to the inverse Kolmogorov scale in the same domain, where the mean radius of curvature scales in a manner similar to the Taylor microscale, whereas both these two length scales

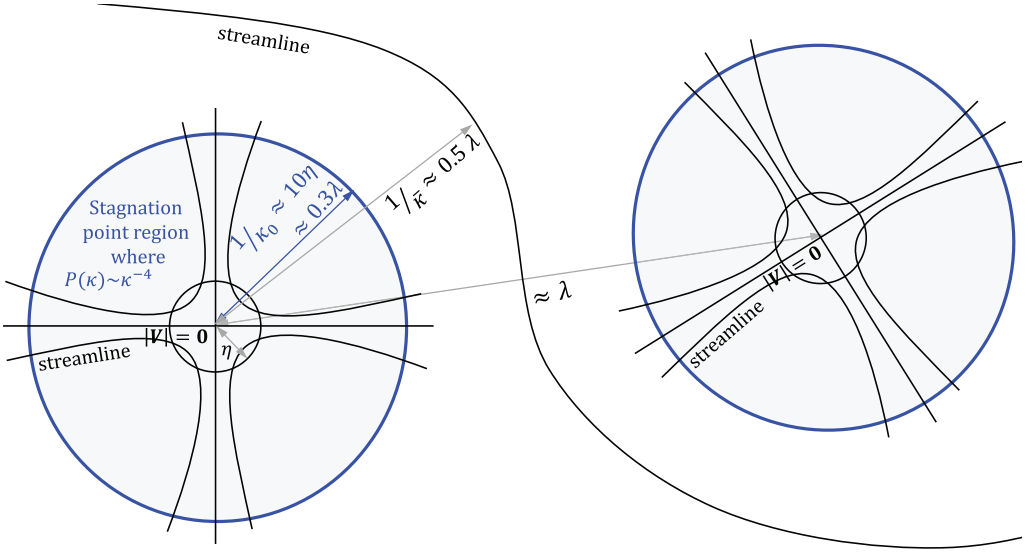

FIG. 16. Sketch of streamlines in the vicinity of a pair of stagnation regions for wall-turbulent flows within the inertial region. The spacing between these points is $\approx\lambda$, whereas the bounding turbulent motion has a size of $1/\bar{\kappa}$. The gray shaded region within the solid blue circle around the stagnation points of size $1/\kappa_0$ is where we expect the curvature pdf $P(\kappa) \sim \kappa^{-4}$ scaling. The streamlines curve sharply deflected within a smaller region of size η.

follow a power-law decrease with y^+. Furthermore, since the distance between the stagnation points on the x-z plane as well as the mean curvature of the streamlines follow the Taylor-microscale, the average streamlines would go between the stagnation points (cf. Fig. 16). Overall, the present results indicate likely connections between the vortical features around the stagnation point of the flow and their spatial structure with distance from the wall.

ACKNOWLEDGMENTS

The authors are grateful to the Australian Research Council (ARC) for the financial support of this research. We are also thankful to Sillero *et al.* [33] and Del Alamo *et al.* [34] for making their DNS data sets available.

APPENDIX: SCALING OF CURVATURE PDFS WITH η AND y

The purpose of this Appendix is to show the PDFs of $\tilde{\kappa}$ as well as κ scaled with the Kolmogorov length scale η as well as with the wall-normal distance y. Figures 17(a) and 17(b) show the PDFs $\tilde{\kappa}$ and κ scaled with η_ϵ (which is the Kolmogorov length scale obtained from the dissipation, ϵ, with no approximation). Figures 17(c) and 17(d) are a replotting of the same data in Figs. 17(a) and 17(b) with y as the normalization. It is clear that the top-row with η_ϵ normalization scales the PDFs better compared to y in the bottom row. Perhaps this is not surprising because the curvature is related to small-scale features of the flow, which typically scale with the Kolmogorov length scale.

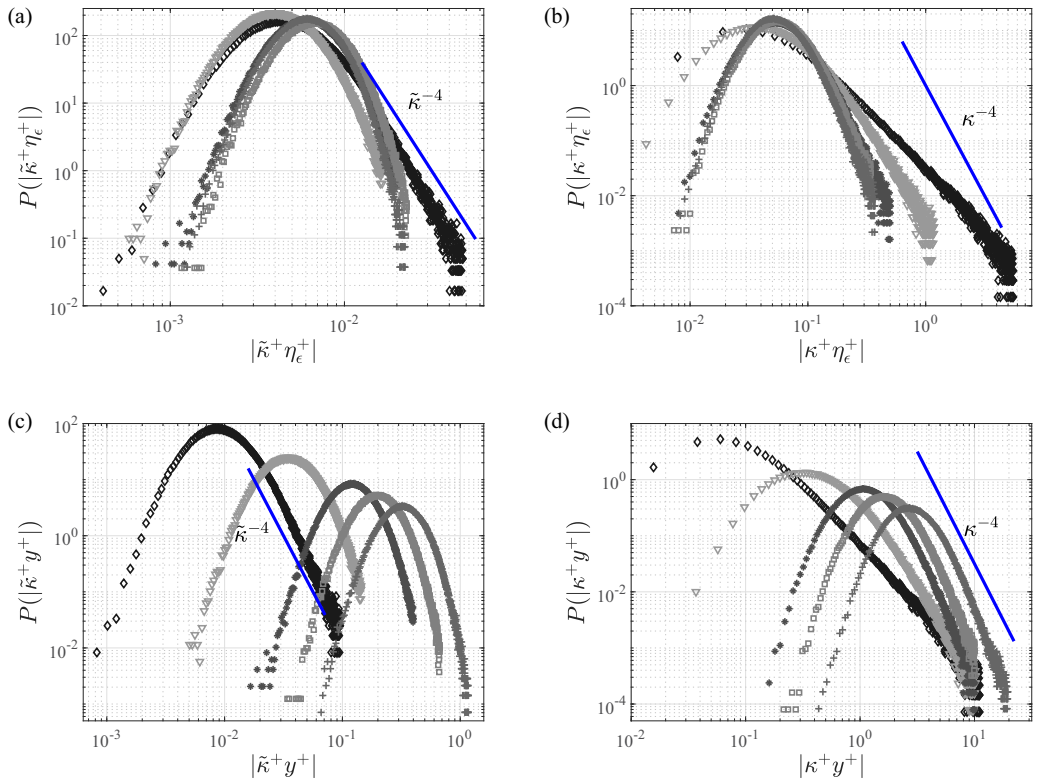

FIG. 17. Probability density function of the curvature magnitude multiplied by Kolmogorov length scale and wall-normal distance for Channel flow at $\delta^+ \approx 934$ at varying wall-normal locations; diamond, $y^+ = 3$; triangle, $y^+ = 14$, star, $y^+ = 40$, square, $y^+ = 67$; plus, $y^+ = 174$. (a) Probability of the curvature magnitude multiplied by Kolmogorov length scale computed from the instantaneous streamlines pattern. (b) Probability of the curvature magnitude multiplied by Kolmogorov length scale for the fluctuating streamlines pattern. (c) Probability of the curvature magnitude multiplied by the wall-normal distance for the instantaneous streamlines pattern. (d) Probability of the curvature magnitude multiplied by the wall-normal distance determined from the fluctuating streamlines pattern.

[1] S. K. Robinson, Coherent motions in the turbulent boundary layer, Annu. Rev. Fluid Mech. **23**, 601 (1991).

[2] I. Marusic, B. J. McKeon, P. A. Monkewitz, H. Nagib, A. Smits, and K. Sreenivasan, Wall-bounded turbulent flows at high Reynolds numbers: Recent advances and key issues, Phys. Fluids **22**, 065103 (2010).

[3] J. Klewicki, Reynolds number dependence, scaling, and dynamics of turbulent boundary layers, J. Fluids Eng. **132**, 094001 (2010).

[4] J. Jeong, F. Hussain, W. Schoppa, and J. Kim, Coherent structures near the wall in a turbulent channel flow, J. Fluid Mech. **332**, 185 (1997).

[5] A. Sharma and B. McKeon, On coherent structure in wall turbulence, J. Fluid Mech. **728**, 196 (2013).

[6] J. Klewicki, J. Philip, I. Marusic, K. Chauhan, and C. Morrill-Winter, Self-similarity in the inertial region of wall turbulence, Phys. Rev. E **90**, 063015 (2014).

[7] P. Schaefer, Curvature statistics of streamlines in various turbulent flows, J. Turbul. **13**, N28 (2012).

[8] V. Dallas, J. C. Vassilicos, and G. F. Hewitt, Stagnation point von Kármán coefficient, Phys. Rev. E **80**, 046306 (2009).
[9] T. Wei, P. Fife, J. Klewicki, and P. McMurtry, Properties of the mean momentum balance in turbulent boundary layer, pipe and channel flows, J. Fluid Mech. **522**, 303 (2005).
[10] C. Morrill-Winter, J. Philip, and J. Klewicki, An invariant representation of mean inertia: Theoretical basis for a log law in turbulent boundary layers, J. Fluid Mech. **813**, 594 (2017).
[11] J. Klewicki, A description of turbulent wall-flow vorticity consistent with mean dynamics, J. Fluid Mech. **737**, 176 (2013).
[12] K. A. Chauhan, P. A. Monkewitz, and H. M. Nagib, Criteria for assessing experiments in zero pressure gradient boundary layers, Fluid Dyn. Res. **41**, 021404 (2009).
[13] J. Klewicki, P. Fife, and T. Wei, On the logarithmic mean profile, J. Fluid Mech. **638**, 73 (2009).
[14] I. Marusic, J. P. Monty, M. Hultmark, and A. J. Smits, On the logarithmic region in wall turbulence, J. Fluid Mech. **716**, R3 (2013).
[15] J. Klewicki and M. Oberlack, Finite Reynolds number properties of a turbulent channel flow similarity solution, Phys. Fluids **27**, 095110 (2015).
[16] C. Meneveau and I. Marusic, Generalized logarithmic law for high-order moments in turbulent boundary layers, J. Fluid Mech. **719**, R1 (2013).
[17] A. Zhou and J. Klewicki, Properties of the streamwise velocity fluctuations in the inertial layer of turbulent boundary layers and their connection to self-similar mean dynamics, Int. J. Heat Fluid Flow **51**, 372 (2015).
[18] C. Morrill-Winter, J. Philip, and J. Klewicki, Statistical evidence of anasymptotic geometric structure to the momentum transporting motions in turbulent boundary layers, Philos. Trans. R. Soc. A **375**, 20160084 (2017).
[19] J. Klewicki, P. Fife, T. Wei, and P. McMurtry, A physical model of the turbulent boundary layer consonant with mean momentum balance structure, Philos. Trans. R. Soc. London A **365**, 823 (2007).
[20] G. L. Eyink, Turbulent flow in pipes and channels as cross-stream "inverse cascades" of vorticity, Phys. Fluids **20**, 125101 (2008).
[21] P. Priyadarshana, J. Klewicki, S. Treat, and J. Foss, Statistical structure of turbulent-boundary-layer velocity–vorticity products at high and low Reynolds numbers, J. Fluid Mech. **570**, 307 (2007).
[22] C Morrill-Winter and J Klewicki, Influences of boundary layer scale separation on the vorticity transport contribution to turbulent inertia, Phys. Fluids **25**, 015108 (2013).
[23] S. Goto and J. C. Vassilicos, The dissipation rate coefficient of turbulence is not universal and depends on the internal stagnation point structure, Phys. Fluids **21**, 035104 (2009).
[24] N. Peters, L. Wang, J.-P. Mellado, J. H. Gobbert, M. Gauding, P. Schafer, and M. Gampert, Geometrical properties of small scale turbulence, in *John von Neumann Institute for Computing NIC Symposium* Edited by G. Münster, D. Wolf, M. Kremer (Jülich, Germany; Forschungszentrum Jülich GmbH, 2010), pp. 365–371.
[25] W. Braun, F. De Lillo, and B. Eckhardt, Geometry of particle paths in turbulent flows, J. Turbul. **7**, N62 (2006).
[26] A. Scagliarini, Geometric properties of particle trajectories in turbulent flows, J. Turbul. **12**, N25 (2011).
[27] P. Huerre and P. A Monkewitz, Local and global instabilities in spatially developing flows, Annu. Rev. Fluid Mech. **22**, 473 (1990).
[28] E Lévêque, L Chevillard, J-F Pinton, S Roux, A Arnéodo, and N Mordant, Lagrangian intermittencies in dynamic and static turbulent velocity fields from direct numerical simulations, J. Turbul. **8**, N3 (2007).
[29] L. Wang, On properties of fluid turbulence along streamlines, J. Fluid Mech. **648**, 183 (2010).
[30] N. Mazellier and J. C. Vassilicos, The turbulence dissipation constant is not universal because of its universal dependence on large-scale flow topology, Phys. Fluids **20**, 015101 (2008).
[31] KR Sreenivasan, A Prabhu, and R Narasimha, Zero-crossings in turbulent signals, J. Fluid Mech. **137**, 251 (1983).
[32] S. O. Rice, Mathematical analysis of random noise, Bell Syst. Tech. J. **24**, 46 (1945).

[33] J. A. Sillero, J. Jiménez, and R. D. Moser, One-point statistics for turbulent wall-bounded flows at Reynolds numbers up to $\delta^+ \approx 2000$, Phys. Fluids **25**, 105102 (2013).
[34] J. C. Del Alamo, J. Jiménez, P. Zandonade, and R. D. Moser, Scaling of the energy spectra of turbulent channels, J. Fluid Mech. **500**, 135 (2004).
[35] R. S. Millman and G. D. Parker, *Elements of Differential Geometry* (Prentice-Hall, Englewood Cliffs, N.J., 1977).
[36] H. Tennekes and J. L. Lumley, *A First Course in Turbulence* (MIT Press, Cambridge, MA, 1972).
[37] J. Klewicki and R. Falco, On accurately measuring statistics associated with small-scale structure in turbulent boundary layers using hot-wire probes, J. Fluid Mech. **219**, 119 (1990).
[38] P. Vincenti, J. Klewicki, C. Morrill-Winter, C. White, and M. Wosnik, Streamwise velocity statistics in turbulent boundary layers that spatially develop to high Reynolds number, Exp. Fluids **54**, 1629 (2013).
[39] A. V Johansson, P H. Alfredsson, and J. Kim, Evolution and dynamics of shear-layer structures in near-wall turbulence, J. Fluid Mech. **224**, 579 (1991).
[40] J. Klewicki and C. Hirschi, Flow field properties local to near-wall shear layers in a low Reynolds number turbulent boundary layer, Phys. Fluids **16**, 4163 (2004).
[41] C. Chin, J. Philip, J. Klewicki, A. Ooi, and I. Marusic, Reynolds-number-dependent turbulent inertia and onset of log region in pipe flows, J. Fluid Mech. **757**, 747 (2014).